Check for updates

Phase stability, electronic, mechanical, lattice distortion, and thermal properties of complex refractory-based high entropy alloys TiVCrZrNbMoHfTaW with varying elemental ratios†

Sahib Hasan, [ab] Puja Adhikari,[a] Saro San[a] and Wai-Yim Ching [*a]

This study examines the intricate area of refractory-based high entropy alloys (RHEAs), focusing on a series of complex compositions involving nine diverse refractory elements: Ti, V, Cr, Zr, Nb, Mo, Hf, Ta, and W. We investigate the phase stability, bonding interactions, electronic structures, lattice distortions, mechanical, and thermal properties of six RHEAs with varying elemental ratios using VASP and OLCAO DFT calculations. Through comprehensive analysis, we investigate the impact of elemental variations on the electronic structure, interacting bond dynamics, lattice distortion, thermodynamic, mechanical, and thermal properties within these RHEAs, providing an insight into how these specific elemental variations in composition give rise to changes in the calculated properties in ways that would guide future experimental and computational efforts. The correlation between the lattice distortion, mechanical, and thermal properties is explored in detail in this work. Our findings reveal significant insights into how these factors contribute to the unique properties of RHEAs, such as enhanced strength, ductility, and resistance to corrosion and wear. This research not only advances our understanding of the fundamental aspects of RHEAs but also opens new avenues for the design and application of these materials in various industrial sectors.

1 Introduction

High Entropy Alloys (HEAs) represent a remarkable class of materials that have fascinated the materials science community due to their unique combination of properties, which include exceptional strength,[1] ductility,[2] corrosion resistance,[3] high-temperature stability,[4,5] fatigue resistance,[6,7] high wear resistance,[8] dielectric,[9] and superconducting[10] properties. HEAs concept was proposed for the first time in 2004 by Yeh *et al.*[11,12] An alloy with entropy larger than $1.5R$ where R is the gas constant (8.3144 J K^{-1} mol^{-1}), is considered a HEA.[13–15] HEAs can provide a significant performance and efficiency in many applications, such as aerospace propulsion systems, gas turbines, nuclear reactors, heat exchangers, and rocket engine nozzles.[16–18] These materials are unique for their multi-principal element composition, unlike conventional alloys with one or two major constituents. Traditional alloys obviously no longer meet the growing demands of rapidly advancing technologies. The concept of high entropy stabilizes the solid solution phase,

leading to novel microstructures and properties that cannot be seen in traditional alloys, such as the so-called cocktail effect and significant lattice distortion.[19,20] The cocktail effect describes any emergent property that cannot be described by the presence of any individual components of HEA. On the other hand, the severe lattice distortion in HEAs is caused by the randomly distributed mismatch of ionic mass and sizes.[21] The variation in bond energy, bond length, and bond strength between the components in HEAs can also lead to severe lattice distortion[22] that ultimately impacts some of their properties such as thermoelectric (TE) properties.[23] Such severe lattice distortion increases the phonons scattering, thus reducing the lattice thermal conductivity (κ_{L}).[11,24,25] Large numbers of distributed solute atoms (more than 5 atoms) with different atomic sizes and characteristics result in distorted lattices with large long-range lattice friction,[2,26,27] which reduces the mobility of phonons and dislocations in HEAs. Hence, the lattice distortion may cause an increase in the yield strength of the solid solution alloys even with very small changes in the microstructure.[28]

A single-phase solid-solution alloy containing multi-principal elements with equimolar or near-equimolar atomic ratios is the original definition of HEAs.[29] HEAs have been extended to include refractory-based high-entropy alloys (RHEAs) by Senkov *et al.*[30,31] Refractory elements such as

aDepartment of Physics and Astronomy, University of Missouri-Kansas City, Kansas City, MO 64110, USA. E-mail: chingw@umkc.edu

bDepartment of Sciences, College of Basic Education, Al Muthanna University, Samawah 66001, Iraq

† Electronic supplementary information (ESI) available. See DOI: https://doi.org/10.1039/d4ra07460b

rhenium (Re), tungsten (W), molybdenum (Mo), tantalum (Ta), niobium (Nb), hafnium (Hf), titanium (Ti), chromium (Cr), and zirconium (Zr) are the main constituents in this type of HEA.[13] To improve the properties, some non-refractory light elements, such as Al and Ni, can also be included to design RHEAs with less density for some applications.[32] Senkov *et al.* found that MoNbTaW, MoNbTaVW, and TaNbHfZrTi have higher melting temperature than the traditional alloys with yield strength of 1058 MPa and 1246 MPa at room temperature. Senkov's alloys also possessed an excellent yield strength of 405 MPa and 477 MPa at high temperature (1600 °C), which is considered much better than that of nickel-based alloys, making them promising materials for high-temperature applications.[33] Due to the potential slow diffusion of refractory elements and solid-solution strengthening, RHEAs keep its remarkable strengths even at elevated temperatures.[13,29,34] After Senkov *et al.*, many RHEAs were developed, however, most of these RHEAs exhibited limited ductility or negligible tensile ductility at room-temperature,[35–37] except for HfNbTaTiZr with BCC structure which exhibits good tensile ductility at room temperature.[38] Due to their constituent elements, such as Ta, Nb, Ti, and Mo, which could form passive films in corrosive environment, RHEAs are considered promising materials for their excellent corrosion resistance.[39–41] Another RHEAs such as TiZrNbTaMo, AlNb-TiVZrx, and MoNbTaTiW have been extensively studied for their excellent mechanical properties.[42–44] RHEAs possessing a single body centered cubic (BCC) structure have much better mechanical properties than other HEAs with face centered cubic (FCC) structure.

The present study focuses on a specific group of RHEAs composed of nine elements: titanium (Ti), vanadium (V), chromium (Cr), zirconium (Zr), niobium (Nb), molybdenum (Mo), hafnium (Hf), tantalum (Ta), and tungsten (W). These elements were chosen for their diverse atomic sizes, valency, and electron configurations, which contribute to the complex microstructure and properties of the resulting alloys. By manipulating the ratios of these elements, we aim to explore the complicated balance between high entropy effects, lattice distortion, mechanical, thermal, and electronic structure contributions in the behaviour of these materials. This investigation is structured around several key areas of interest. Firstly, we test the phase stability of these six alloys *via* study thermodynamic parameters and other affecting factors such as entropy of mixing (ΔS_{mix}), enthalpy of mixing (ΔH_{mix}), change in Gibbs free energy (ΔG_{mix}), valence electron concentration (VEC), the atomic size difference (δ), and electronegativity difference ($\Delta\chi$). Secondly, the electronic structure of these complex alloys is studied to provide insights into the role of electron behaviour in determining overall material properties. Thirdly, the study examines into the atomic-scale interactions, focusing on bond order (BO), a measure of the bond strength, and total bond order density (TBOD), to clarify the role of electron density distribution in defining the materials structural stability and mechanical characteristics. TBOD is a single quantum mechanical metric to describe the internal cohesion of the RHEA. Fourthly, we examine the mechanical properties of these RHEAs, such as bulk modulus, Young modulus, shear modulus,

Pugh ratio, Vickers hardness, Cauchy pressure, and machinability index, and their correlation with TBOD to understand how the high entropy nature contributes to their enhanced performance. Lattice distortion (LD), an assurance feature of RHEAs, is analysed in relation to its impact on dislocation movement and, consequently, mechanical and thermal properties. Finally, we study the thermoelectric (TE) performance of RHEAs models by calculating several crucial parameters such as Debye temperature, minimum thermal conductivity, Grüneisen parameter, lattice thermal conductivity, melting temperature, and thermal expansion. Then we analyze the effect of LD and Grüneisen parameter on lattice thermal conductivity. By systematically exploring these aspects, the current study aims to contribute significantly to the fundamental understanding of RHEAs, thereby guiding the development of new materials with tailored properties for advanced applications in aerospace, automotive, and energy sectors, among others.

2 Computational methods

The initial model of the RHEA was developed using a Nb Body-Centered Cubic (BCC) unit cell, identified by space group 229. This model was then enhanced through the incorporation of various refractory metals (Ti, V, Cr, Zr, Nb, Mo, Hf, Ta, and W) using a random ratio including equiatomic and non-equiatomic RHEAs. A specialized Python script was used to determine the lattice parameters, considering the inclusion of these transition metals within their specific cells. This Python script is available in the ESI file.† To simulate a disordered atomic arrangement, we constructed $8 \times 8 \times 8$ supercells of BCC structure, leading to the formation of six RHEAs random solid solutions containing 1024 atoms each. For TiVCrZrNbMoHfTaW, two configurations (m1 and m2) were studied, while one structure was studied for each of the remaining four compositions. The ball and stick figure for m1 is shown in Fig. 1. These six distinct RHEA models (listed in Table 1) were subsequently optimized using the Vienna *Ab* initio Simulation Package (VASP).[45] VASP optimizations employed the Projector Augmented Wave (PAW) of
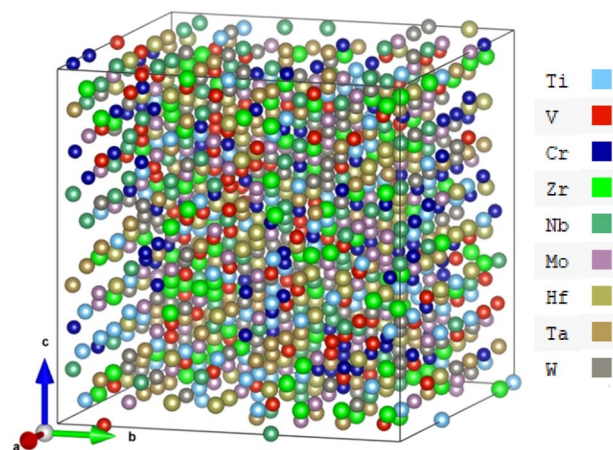

Fig. 1 Ball and stick structure of TiVCrZrNbMoHfTaW (m1) solid solution.

Table 1 Composition, lattice parameters, volume of the supercell, first (NN), and second (SNN) nearest neighbors distances of various TiVCrZrNbMoHfTaW system

Model	Composition	a, b, c (Å)	α, β, γ in deg.	Vol (Å^3)	NN (Å)	SNN (Å)
m1	TiVCrZrNbMoHfTaW	25.9, 25.9, 25.8	89.9, 90.2, 90.1	17 386.70	2.804	3.238
m2	TiVCrZrNbMoHfTaW	25.9, 25.9, 25.9	90.2, 89.9, 89.8	17 391.71	2.805	3.239
m3	Ti$_{114}$V$_{114}$Cr$_{138}$Zr$_{90}$Nb$_{114}$Mo$_{138}$Hf$_{90}$Ta$_{113}$W$_{113}$	25.7, 25.8, 25.7	89.9, 90.2, 90.1	16 957.03	3.211	2.781
m4	Ti$_{164}$V$_{65}$Cr$_{118}$Zr$_{118}$Nb$_{99}$Mo$_{118}$Hf$_{104}$Ta$_{119}$W$_{119}$	26.1, 25.9, 25.9	90.2, 89.9, 90.0	17 510.73	3.246	2.811
m5	Ti$_{114}$V$_{114}$Cr$_{171}$Zr$_{57}$Nb$_{114}$Mo$_{171}$Hf$_{57}$Ta$_{113}$W$_{113}$	25.4, 25.4, 25.4	90.1, 90.2, 90.2	16 381.24	2.749	3.175
m6	Ti$_{114}$V$_{114}$Cr$_{228}$Nb$_{114}$Mo$_{228}$Ta$_{113}$W$_{113}$	24.9, 24.9, 24.9	90.0, 90.0, 90.1	15 430.82	2.695	3.112

Perdew, Burke, and Ernzerhof (PBE)[46] method within the Generalized Gradient Approximation (GGA) to address the exchange-correlation potential. We selected the plane wave expansion kinetic energy cutoff of 500 eV, with the electronic and ionic relaxations requiring convergence thresholds of 1.0×10^{-6} eV and -1.0×10^{-4} eV Å^{-1}, respectively. The Monkhorst scheme[47] is used with k-point meshes of $1 \times 1 \times 1$ for all these RHEAs solid solutions. The optimized structures from VASP were used to calculate the elastic tensors by employing a stress–strain response approach. The calculation of the elastic coefficient C_{ij} matrix involved solving a linear equation where the stress σ_i is a function of the applied strains ε_j. This linear equation, also called the Hooke's law:[48,49]

$$\sigma_i = \sum_{j=1} C_{ij}\varepsilon_j \tag{1}$$

Eqn (1) can be solved to obtain the elastic coefficient, C_{ij}, with both indices ranging from 1 to 6, at strains of $\pm 0.50\%$. From these C_{ij} matrices, bulk modulus (K), shear modulus (G), Young's modulus (E), and Poisson's ratio (η) were derived using the Voigt–Reuss–Hill (VRH) approximation,[50,51] which is applicable to polycrystalline materials. More details on mechanical properties calculation are described in ESI.† The Orthogonalized Linear Combination of Atomic Orbitals (OLCAO)[52] technique was applied to investigate the electronic structure and chemical bonding, using the structure refined by VASP as the starting point. OLCAO method, which is an all-electron approach, uses the local density approximation (LDA) as the exchange and correlation potential. OLCAO utilizes Gaussian-type orbitals (GTO) to form the atomic orbitals that are part of the basis set for expanding the Bloch functions. OLCAO has been successfully applied in DFT calculations of both crystalline,[53–59] non-crystalline materials,[60,61] HEAs,[62,63] and complex bio-molecular systems.[64,65] A $1 \times 1 \times 1$ Monkhorst k-points mesh was used for OLCAO density of states (DOS) calculations. Within this framework, OLCAO determines the bond order (BO) and effective charge (Q^*) metrics, drawing on Mulliken's analysis.[66] The bond order, indicative of bond strength, is calculated as the overlap population $\rho_{\alpha,\beta}$ between atom pairs (α,β) at a given bond length:

$$\rho_{\alpha\beta} = \sum_{n, \text{occ}} \sum_{i,j} C_{i\alpha}^{*n} C_{j\beta}{}^n S_{i\alpha, j\beta} \tag{2}$$

The formula for $\rho_{\alpha\beta}$ involves summing over occupied bands (n,occ) and integrating the product of the complex conjugate of

the coefficient $C_{i\alpha}^{*n}$, the coefficient $C_{j\beta}{}^n$, and the overlap integral $S_{i\alpha,j\beta}$ across the orbital indices i and j. For effective charge Q_α^*, the calculation aggregates the products of eigenvector coefficients and the overlap integrals over all bands and orbitals, reflecting the charge distribution deviation from a neutral state. Additionally, the partial charge (PC) for each atom was assessed in every model, defined as the difference between the effective (Q_α^*) and neutral atomic charges (Q_α^0).

$$Q_\alpha^* = \sum_{i,j,\beta} \sum_{n,\text{occ}} C_{i\alpha}^{*n} C_{j\beta}^n S_{i\alpha,j\beta} \tag{3}$$

The aggregation of all bond orders within a model yields the total bond order (TBO), which, when normalized by the model's volume, provides the total bond order density (TBOD). TBOD serves as a quantum mechanical measure of the alloy's structural integrity.[67] The optimized structure parameters along with first and second nearest neighbors are listed in Table 1. Notice that the only difference between model m1 and model 2 is the way that these nine elements are distributed in the model.

3 Results and discussion

3.1. Parameters affecting RHEAs formation

The Hume-Rothery rules[68,69] play a crucial role in predicting phase formation of HEAs. These rules are based on enthalpy of mixing, atomic-size difference, electronegativity difference, and valence electron concentration. The formation of HEAs is inevitably linked to the energy of the system, so thermodynamic factors are vital for the study and design of HEAs when discussing their formation process. Thermodynamic parameters can predict the phase of the HEAs. The first three principal components that affect the phase formation are: the entropy of mixing (ΔS_{mix}), enthalpy of mixing (ΔH_{mix}), and Gibbs free energy (ΔG_{mix}):[70]

$$\Delta S_{\text{mix}} = -R \sum_{i=1}^{n} c_i \ln c_i \tag{4}$$

$$\Delta H_{\text{mix}} = \sum_{i=1,i\neq j}^{n} 4 c_i c_j \Delta H_{\text{mix}}^{\text{AB}} \tag{5}$$

$$\Delta G_{\text{mix}} = \Delta H_{\text{mix}} - T\Delta S_{\text{mix}} \tag{6}$$

R is the molar gas constant, $R = 8.314$ J (mol^{-1} K^{-1}), n is the number of components of the multi-component material, c_i and c_j are the content or atomic fraction of the ith and jth components (at%) (as listed in Table S1† for the six RHEAs). ΔH_{mix}^{AB} is the enthalpy of mixing of a two-element (A–B) liquid alloy calculated based on the Miedema's model[71] and T is the absolute temperature in Kelvin unit. Formation of single-phase solid solutions favors low magnitude of ΔH_{mix}. Thus ΔH_{mix} needs to be considered in the formation of solid solution phase. ΔS_{mix} increases with increase the number of components, and thus reduces ΔG_{mix} of the solid solution. Reducing ΔG_{mix} renders the solid solution more thermodynamically stable and promotes the formation of single-phase HEA. However, some studies[72,73] showed that secondary phases such as intermetallic compounds can be formed in HEAs even at high ΔS_{mix}. Besides ΔS_{mix}, ΔH_{mix}, and ΔG_{mix}, the parameter Ω was proposed to predict whether an alloy is solid soluted by quantifying the dominance of entropy to enthalpy. Ω is defined as a ratio of the product of ΔS_{mix} and the melting temperature to the absolute value of ΔH_{mix} of HEAs:[74]

$$\Omega = \frac{T_m \Delta S_{mix}}{|\Delta H_{mix}|} \quad (7)$$

where T_m is the average melting temperature in Kelvin of the alloy. Using the rule of mixtures, T_m is given by:

$$T_m = \sum_{i=1}^{N} c_i (T_m)_i \quad (8)$$

where $(T_m)_i$ is the melting point for the ith element. The atomic radius,[75] elemental valence electron concentration (VEC),[76,77] elemental Pauling electronegativity($\chi_{Pauling}$),[76,77] elemental Allen electronegativity(χ_{Allen}),[76] and elemental melting point (T_m) in Kelvin[77] of Ti,V, Cr, Zr, Nb, Mo, Hf, Ta, and W elements are listed in Table S2.† To obtain a single-phase HEA, ΔH_{mix} and ΔS_{mix} should be in the ranges: -22.0 kJ mol$^{-1} \leq \Delta H_{mix} \leq 7.0$ kJ mol^{-1} and 11.0 J (K^{-1} mol^{-1})$^{-1} \leq \Delta S_{mix} \leq 19.5$ J (K^{-1} mol^{-1}), respectively.[78] While amorphous phases form at more negative ΔH_{mix} (-49.0 kJ mol$^{-1} \leq \Delta H_{mix} \leq -5.5$ kJ mol^{-1}).[78] Guo et al.[79] suggested that disordered solid solution may form when -5 kJ mol$^{-1} \leq \Delta H_{mix} \leq 5$ kJ mol^{-1}, while intermetallic compounds would form once ΔH_{mix} is more negative. From Table 2, the values of ΔS_{mix} and ΔH_{mix} for these six RHEAs meet these criteria and they may form single-phase solid solutions. On the other hand, Ω should be roughly larger than 1.1, so the contribution from $T\Delta S_{mix}$ in eqn (6) is larger than the

contribution from ΔH_{mix}. Thus, the HEA is mainly composed of the solid solutions. If $\Omega < 1.0$, ΔH_{mix} value will dominate ΔG_{mix} and thus, intermetallic compounds and segregations are prior to solid-solution phases to form HEAs.[74] The larger the Ω, the stronger the high-entropy effect, and thus, the higher the probability of forming a single-phase random solid solution in HEAs and vice versa. The calculated Ω are listed in Table S3.† All six RHEAs have high Ω (~9) indicating forming a single BCC solid solution.

When all constituent atoms (with different sizes) of a HEA are placed together in a certain lattice, a severely distorted lattice results from the presence of large atomic size difference. In 2008, Zhang et al.[70] suggested a new parameter, namely, the atomic size difference (δ), to characterize such an atomic size effect in HEAs as follows:

$$\delta = 100 \sqrt{\sum_{i=1}^{n} c_i \left(1 - \frac{r_i}{\bar{r}}\right)^2} \quad (9)$$

with $\bar{r} = \sum_{i=1}^{N} c_i r_i$. Experimentally, the formation of metallic glasses favors larger values of δ (~$\delta > 11$%) while HEAs formation favors less values of δ. δ is widely used nowadays to predict the formation of HEAs. However, the value of δ cannot give an accurate estimation of local lattice distortions. Yang and Zhang[74] suggested a critical condition for solid solution formation which is $\delta \leq 6.6$. Multicomponent systems with higher δ than critical condition may form intermetallic compounds. Guo et al. and Nutor et al. showed that solid solution phases can form when the parameter δ is in the range: $0 \leq \delta \leq 8.5$,[80] while bulk metallic glasses form in the region $\delta \geq 9$.[78] δ for the six RHEAs is listed in Table 2. All these six RHEAs have large values of δ (~7). Dong et al. and Poletti et al.[81,82] showed that HEAs with high δ (~7) form laves phase plus BCC solid solutions phase. From Zhang et al.'s work,[29] HEAs having large δ (~7) form solid solutions plus intermetallic compounds. Thermodynamic approach can be combined with the geometrical information (lattice characteristics and atomic radius) by the parameter $\wedge$. Singh et al.[83] developed the $\wedge$ parameter (named the combination parameter) to predict the formation of disordered solid solution as follows:

$$\Lambda = \frac{\Delta S_{mix}}{\delta^2} \quad (10)$$

The main idea of $\wedge$ is that high ΔS_{mix} and low δ stabilize the single-phase solid solution. According to Singh's proposal for $\wedge$

Table 2 Enthalpy of mixing (ΔH_{mix}), entropy of mixing (ΔS_{mix}), atomic size difference (δ), valence electron concentration (VEC), and average melting temperature (T_m) of various TiVCrZrNbMoHfTaW system

Model	ΔH_{mix} (kJ mol^{-1})	ΔS_{mix} (J.K^{-1} mol^{-1})	δ%	VEC	T_m (K)
m1	−4.790120	18.26669	7.6378	4.99995	2618.42
m2	−4.790120	18.26669	7.6378	4.99995	2618.42
m3	−5.061120	18.19895	7.0564	5.10054	2631.89
m4	−5.000125	18.08030	7.4853	4.97060	2611.79
m5	−5.188510	17.80139	7.3409	5.22854	2646.13
m6	−4.800360	15.71158	7.1213	5.45254	2671.05

parameter, single-phase solid solution requires $\wedge > 0.96$, two phases solid solution form when $0.24 < \wedge < 0.96$, while intermetallic compounds form at $\wedge < 0.24$. The values of $\wedge$ listed in Table S3† are about 0.3 for all models. This may indicate forming another phase along with BCC solid solution phase in these RHEAs. Calculating the valence electron concentration (VEC) is also important to predict the formation of stable crystalline structures and stability for FCC and BCC phases of HEAs.[84] VEC is the total number of valence electrons per atom. VEC can be calculated as follows:[78]

$$VEC = \sum_{i=1}^{n} c_i (VEC)_i \quad (11)$$

where $(VEC)_i$ is the VEC for the ith element. VEC for the six RHEAs is listed in Table 2. In general, high VEC values favor FCC structures, but low VEC values prefer BCC phases. At VEC ≥ 8.0, single FCC solid solution phase exists; at $6.87 \leq VEC < 8.0$, mixed FCC and BCC solid solution phases will co-exist; and at VEC < 6.87, single BCC solid solution phase exists.[4,79,85–91] An experimental study[92] showed that: at VEC ≥ 4.18, a single BCC solid solution phase is formed; mixed BCC and hexagonal close packed (HCP) phases co-exist at $4.09 \leq VEC < 4.18$; while HCP phase can be formed at VEC < 4.09 for TiZrHfNbTa RHEA. According to these criteria, these six RHEAs may form single BCC solid solution phase. Pauling electronegativity difference ($\Delta\chi_{Pauling}$) and Allen electronegativity difference ($\Delta\chi_{Allen}$) parameters can be used to assess the phase formation of HEAs, and they are given by:[78,79,93–95]

$$\Delta\chi_{Pauling} = \sqrt{\sum_{i=1}^{n} c_i \left(\chi_i^{Pauling} - \sum_{j=1}^{n} c_j \chi_j^{Pauling} \right)^2} \quad (12)$$

$$\Delta\chi_{Allen} = \sqrt{\sum_{i=1}^{n} c_i \left(1 - \frac{\chi_i^{Allen}}{\sum_{j=1}^{n} c_j \chi_j^{Allen}} \right)^2} \quad (13)$$

Electronegativity is the ability of atoms to attract charges toward itself.[96] The atoms in a HEA can attract electrons uniformly when the electronegativity difference has low value,

thus stable solid solutions can form. While the formations of amorphous structures favors high electronegativity difference.[97] $\Delta\chi_{Pauling}$ and $\Delta\chi_{Allen}$ for these six RHEAs are listed in Table S3.† These six alloys have uniquely large $\Delta\chi_{Pauling}$ due to the existence of Mo and W elements which have much larger electronegativity than the other elements (see Table S2†). Dong et al.[81] showed that the topologically close-packed (TCP) phases form at $\Delta\chi_{Pauling} > 0.133$. Thus, these six RHEAs may form laves phase and TCP phases along with BCC solid solution. These RHEAs have $\Delta\chi_{Allen}$ higher than 8.0%. Yurchenko et al.[98] showed that the formation of laves phase can be observed at $\Delta\chi_{Allen} > 7.0\%$.

3.2. Electronic structure analysis

These six BCC RHEAs solid solutions are made with varying proportions of components. The new local chemical environment of the different elements: Ti, V, Cr, Zr, Nb, Mo, Hf, Ta, and W results in a huge deformation. Some properties such as electronic structure and interatomic bonding can be affected by this deformation. The electronic structure of a material may reflect the stability of that material. Density of states (DOS) and partial density of states (PDOS) of the models m1 and m6 are demonstrated in Fig. 2, while Fig. S1 in the ESI† contains the figures of DOS and PDOS of all models. The DOS predominantly originated from the 3d orbitals in Ti, V, and Cr, the 4d orbitals in Zr, Nb, and Mo, and the 5d orbitals in Hf, Ta, and W. DOS has no minimum at Fermi energy (E_F) for all models. However, the minimum or dip in DOS of m6 is very close to E_F, which indicates its stability compared to other models. Notably the $N(E_F)$ values in Table 3 show that m5 and m6 a lower dip or minimum in the DOS at E_F. This is because m5 and m6 contain higher percentage of 3d and 4d elements (Cr and Mo).

Table 4 and Fig. S2† show that the highest contributions to the TDOS at E_F in m1 and m2 are from V atom, whereas the highest contributions to the TDOS at E_F in m3 and m4 are from Cr and Ti respectively. The highest contributions to the TDOS at E_F in m5 and m6 are from Cr atom. On the other hand, Table 3 shows that m1 and m2 have the largest values of TDOS at E_F of 1235 state per eV and 1222 state per eV respectively, attributed to the contribution from V. While m6 has the lowest TDOS value
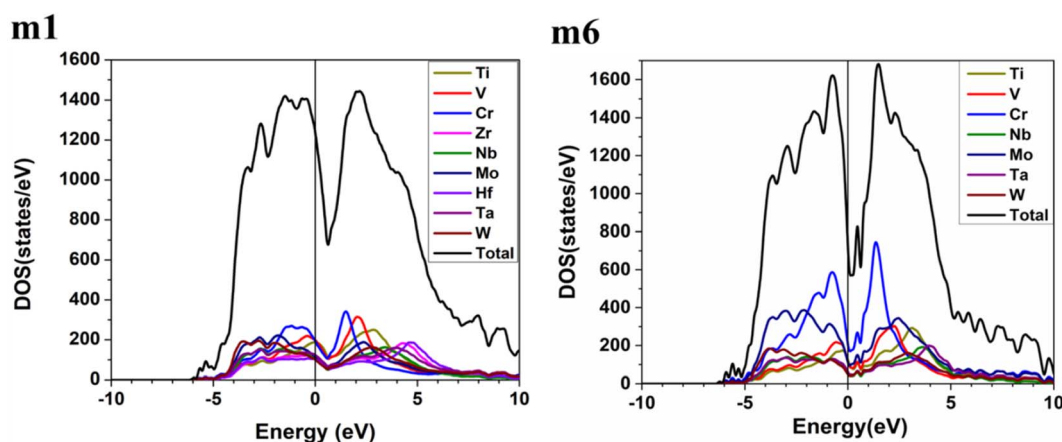

Fig. 2 Calculated total density of states (TDOS) and partial density of states (PDOS) of m1 and m6 RHEAs models from −10 eV to 10 eV.

Table 3 Density of states at the Fermi energy, with identifying of the primary and secondary peaks within the conduction and valence bands of various TiVCrZrNbMoHfTaW system

#	Model	$N(E_F)$	N (first peak)	E (eV)	N (second peak)	E (eV)
1	m1	1235	1420	−1.48	1442	2.12
2	m2	1222	1437	−0.65	1462	1.99
3	m3	1197	1445	−0.53	1466	2.01
4	m4	1140	1447	−0.76	1381	2.29
5	m5	1119	1528	−0.62	1514	1.80
6	m6	732	1620	−0.77	1677	1.52

at E_F of 732 stat per /eV, with $N(E_F)$ of m3, m4, and m5 are somewhere in between. It is well known that $N(E_F)$ is related to the electrical conductivity and m1 and m2 should have higher electrical conductivity than the other four RHEAs models. m6 should have lowest electrical conductivity amongst other RHEAs models.

3.3. Partial charge and interatomic bonding characteristics

The valence electron count (VEC) is a fixed charge quantity for each element in the periodic table regardless of its pure environment and can be used only in that pure environment. On the other hand, the average partial charge (PC) and effective charge (Q^*), calculated using the methods described in Section 2 (Computational methods), are important aspect of the electronic structure and are much more meaningful than VEC. In HEAs, the local environment and structure of a certain atom can significantly change when interacting with other atoms in the complex structure. Thus, the interpretation of VEC in HEAs in some published literature is misleading. The calculated PC and Q^* on each atom in the six RHEAs models are shown in Table 5 and Table 6 respectively. The values of PC and Q^* vary from one model to another depending on their compositions. As shown in Table 5, in general, Ti, Cr, and Mo atoms gain charges in all models, while Zr, Nb, Hf, and Ta atoms lose charges in all models.

W atom loses charges in the models from m3 to m6. V atom gains charges in the models from m1 to m4 and loses charges in m5 and m6. The distribution of the calculated PC for each element in each RHEA model is shown in Fig. 3 for m1 and m6, and Fig. S3 (m1–m6) in the ESI† for all models. The values of PC in Table 5 are average values. However, a closer look at Fig. 3 and S3† indicates that all elements in these six RHEAs models gain and lose charges within the same model in different percentages. As can be seen in Fig. S3,† the PC activity vary in these six RHEAs models. A recent study[99] showed that a larger

Table 4 Partial density of states (PDOS) value at Fermi level of each element in the six RHEAs in unit of state per eV

#	Model	Ti	V	Cr	Zr	Nb	Mo	Hf	Ta	W
1	m1	187.05	190.04	178.96	112.28	100.79	113.68	102.87	124.49	103.22
2	m2	178.76	197.69	190.86	110.55	100.01	104.09	95.24	116.34	87.19
3	m3	177.63	167.31	190.55	77.38	78.88	108.62	74.41	109.89	89.27
4	m4	273.19	113.33	154.62	101.43	93.31	100.81	95.50	105.32	85.32
5	m5	165.06	159.02	225.99	43.13	80.49	120.96	36.92	84.67	68.28
6	m6	125.67	116.41	202.86	—	56.43	113.57	—	62.20	48.49

Table 5 Average partial charge (PC) and VEC for each element in six the RHEAs models

#	Model	Ti	V	Cr	Zr	Nb	Mo	Hf	Ta	W	Q^*_{ave}
1	m1	−0.05	−0.08	−0.68	0.34	0.25	−0.41	0.56	0.06	0	5.0007
2	m2	−0.04	−0.08	−0.72	0.35	0.25	−0.42	0.57	0.07	0	5.0018
3	m3	−0.01	−0.02	−0.66	0.38	0.30	−0.35	0.59	0.13	0.05	5.1026
4	m4	−0.15	−0.16	−0.65	0.41	0.16	−0.34	0.49	0.19	0.11	4.9696
5	m5	−0.05	0.05	−0.63	0.47	0.35	−0.30	0.68	0.21	0.15	5.2305
6	m6	−0.20	0.16	−0.54		0.43	−0.18	—	0.35	0.28	5.4565
7	VEC	4	5	6	4	5	6	4	5	6	

Table 6 Total bond order density (TBOD) and effective charge (Q^*) for each atom in six RHEAs models

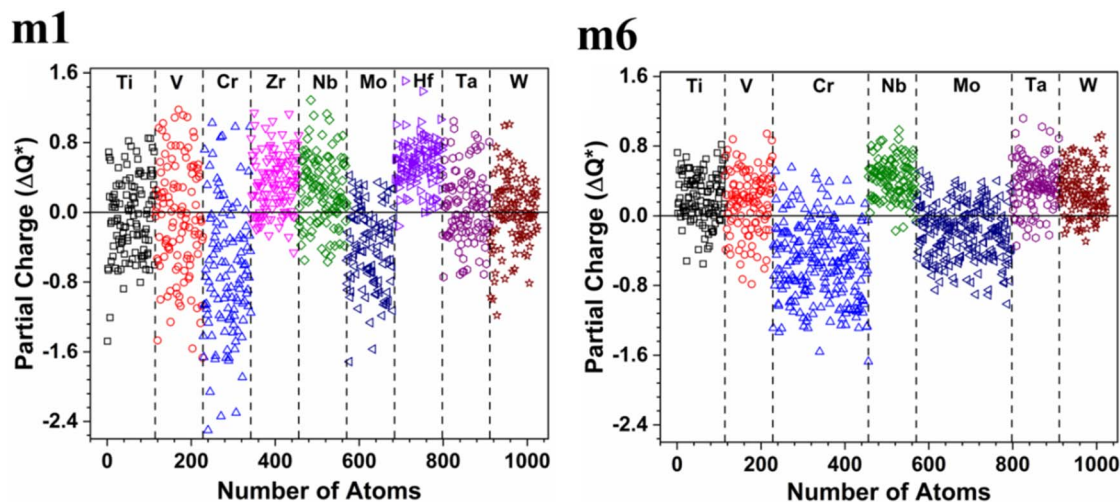| #	Model	TBOD	Average effective charge(Q^*)
1	m1	0.0453	Ti (4.05), V(5.08), Cr (6.68), Zr (3.66), Nb (4.75), Mo (6.41), Hf (3.44), Ta (4.94), W (6)
2	m2	0.0452	Ti (4.04), V(5.08), Cr (6.72), Zr (3.65), Nb (4.75), Mo (6.42), Hf (3.43), Ta (4.93), W (6)
3	m3	0.0472	Ti (4.01), V(5.02), Cr (6.66), Zr (3.62), Nb (4.70), Mo (6.35), Hf (3.41), Ta (4.87), W (5.95)
4	m4	0.0454	Ti (4.15), V(5.16), Cr (6.65), Zr (3.59), Nb (4.84), Mo (6.34), Hf (3.51), Ta (4.81), W (5.89)
5	m5	0.0499	Ti (3.95), V(4.95), Cr (6.63), Zr (3.53), Nb (4.65), Mo (6.30), Hf (3.32), Ta (4.79), W (5.85)
6	m6	0.0547	Ti (3.80), V(4.84), Cr (6.54), Nb (4.57), Mo (6.18), Ta (4.65), W (5.72)

Fig. 3 Distribution of partial charge in m1 and m6 RHEAs models.

PC activity between the elements in a HEA model may indicate a larger lattice distortion. Fig. 3 shows much larger PC activity in m1 than in m6, suggesting increased lattice distortion (LD) in m1 (see Section 3.5). The average overall Q^* of each HEA can be obtained from the formula: $Q_{ave}^* = \sum c_i Q_i^*$, where c_i is the composition of the components. The calculated Q_{ave}^* for each model of the six RHEAs models are listed in Table 5. The highest Q_{ave}^* is in m5 and m6 while the lowest Q_{ave}^* is in m1. These numbers are important for designing HEAs because they correlate with total energy and other properties such as mechanical properties (see Section 3.4). The distribution of the calculated Q^* for each atom in each RHEA model is shown in Fig. 4 for m1 and m6, and Fig. S4† (m1–m6) in the SI for all models. Cr and Mo have the highest Q^* in m1, m2, m3, m5, and m6 whereas Ti has the highest Q^* in m4. Fig. 4 shows that Q^* is much more scattered in m1 than m6 which indicates a higher Q^* activity and thus a larger lattice distortion in m1 than m6 (see Section 3.5).

More details about the nature of interatomic interactions between different elements in these six RHEAs models could be revealed via using bond order (BO) and bond length (BL) data. The distribution of BO versus BL for each model is shown in Fig. S5† while the distribution of BO versus BL for all types of bonds in these six RHEAs models is shown in Fig. S6 in the ESI.† These six RHEAs models are constituted from nine metallic elements (Ti, V, Cr, Zr, Nb, Mo, Hf, Ta, W), Therefore, there is a presence of metallic bonds. To comprehend the formation of these six RHEAs models, it is important to understand the nature of these metallic bonds. The lack of information about the metallic bonding for this class of RHEAs motivated us to investigate this bonding. Sharing the valence electrons of all nearby atoms is the origin of metallic bonds.

As an atom making a bond pair transition from the first nearest neighbour to the next nearest neighbour and beyond, the bond's strength decreases. In metallic bonding, there could be several possible values of BO for one certain distance of separation for a pair of atoms, and there could be many possible
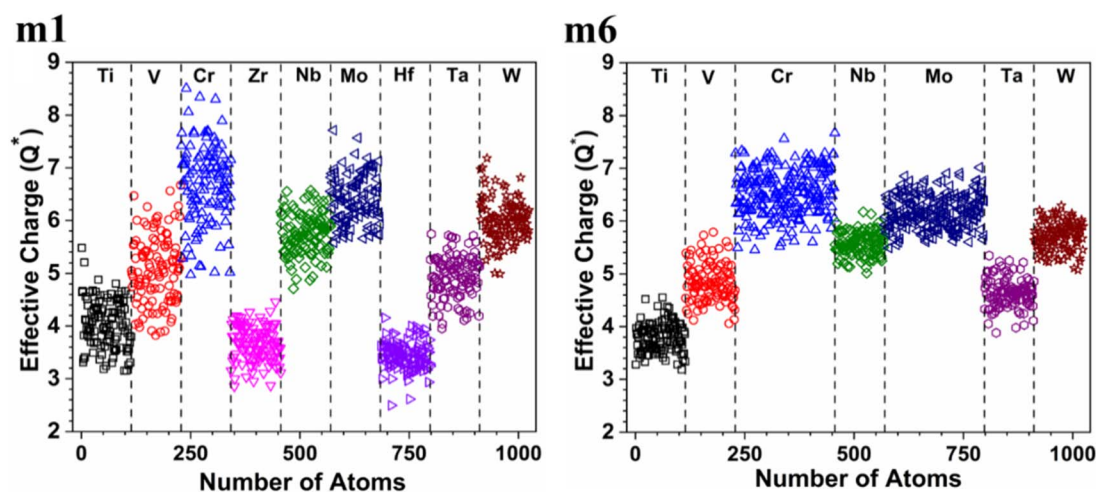

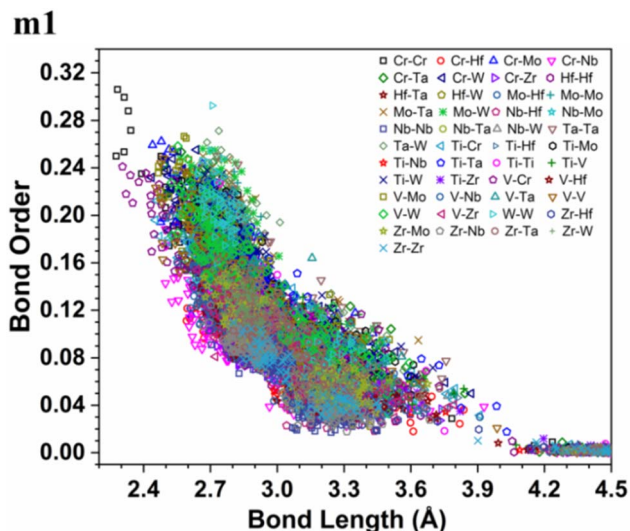Fig. 4 Distribution of effective charge in m1 and m6 RHEAs models.

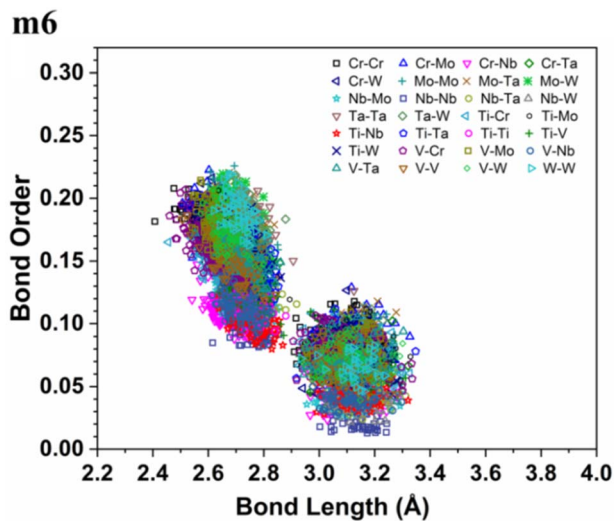**Fig. 5** Bond order (BO) *versus* bond length (BL) distribution in the m1 RHEA model.

Fig. 6 Bond order (BO) *versus* bond length (BL) distribution in the m6 RHEA model.

Fig. 7 Distribution of the TBOD in the RHEAs models as is displayed in bar charts.

pairs of atoms for the same distance of separation. A significant implication of interatomic bonding analysis can provide an opportunity to investigate the lattice distortion (LD) in RHEAs. In Fig. 5, and 6, we plotted BO *versus* BL data for m1 and m6 models. These two figures show that bonds in m1 have much broader distribution than m6 which hints the lattice is much more distorted in m1. Deep analysis of our calculations for BO and BL data and observations can be found in the ESI.†

From these observations in ESI,† we conclude that most bonds in the models from m1 to m4 are scatterd in long BLs indicating larger lattice distortion. In contrast, most bonds in m5 and all bonds in m6 are concentrated or assembled in shorter BLs, indicating small lattice distortion in these two models. In Section 3.5, we discuss lattice distorion in these six RHEAs models in detail. m6 uniquely contains 7 elements
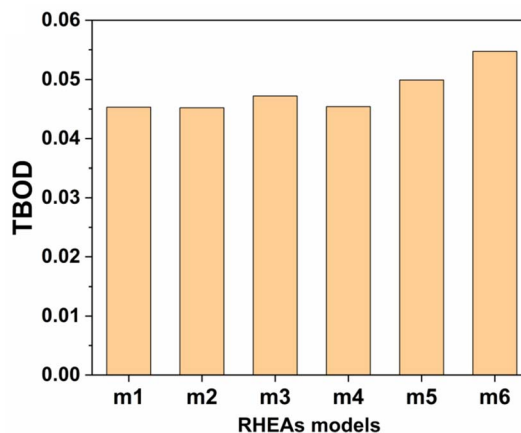
instead of 9, providing an opportunity to investigate the impact of the element count on HEA properties. The summation of all bond order values for all bond pairs in the corresponding RHEA model is called total bond order (TBO). TBO can be normalized by the volume of the cell to obtain the total bond order density (TBOD). TBOD describes the internal cohesion in a HEA model. TBOD values for all RHEAs models are listed in Table 6 and plotted in Fig. 7. Models m1 and m2 have the lowest TBOD whereas m6 has the largest TBOD among other models. To obtain more insights and reveal the details of interatomic interactions in these RHEAs, we resolved the TBOD into partial bond order density (PBOD) based on the volume defined. Quantum mechanical calculations were used to derive both TBOD and PBOD. The PBOD of the six RHEAs models is displayed in the bar charts in Fig. 8 for m1 and m6, and S7† for all models. As can be seen, each type of bond pair has its unique characteristic, and the PBOD of these bond pairs vary among these six models. So, in both figures the *x*-axis is ordered in decreasing order of PBOD. In m1, the highest PBOD is from V–Mo and Ta–W bond pairs. In m2, Ta–W and Cr–Ta pairs have the highest PBOD. In m3, the highest PBOD is from Cr–Ta and V–Mo bond pairs, while Ti–Hf and Ta–W have the highest PBOD in m4. Cr–Mo bonds have the highest PBOD in m5 and m6.

3.4. Mechanical properties

In current work, VASP is used to calculate the mechanical properties of these RHEAs models. The response of a material toward a certain stress is described by the elastic constants. The calculated elastic constants (C_{11}, C_{12}, and C_{44}) are listed in Table 7. The resistance of a material against the deformation along [100] direction can be described by C_{11}. Large value of C_{11} refers to incompressibility under uniaxial stress along *x*-axes. Changing only the elemental distribution in m2 leads to small changes in elastic constants and mechanical moduli whereas noticeable changes in hardness and lattice distortion (see Section 3.5). One of the key factors to manipulate the properties of these alloys is mainly changing (reducing or increasing) the composition (the atomic fractions) of the Cr, Mo, Ti, Zr, and Hf
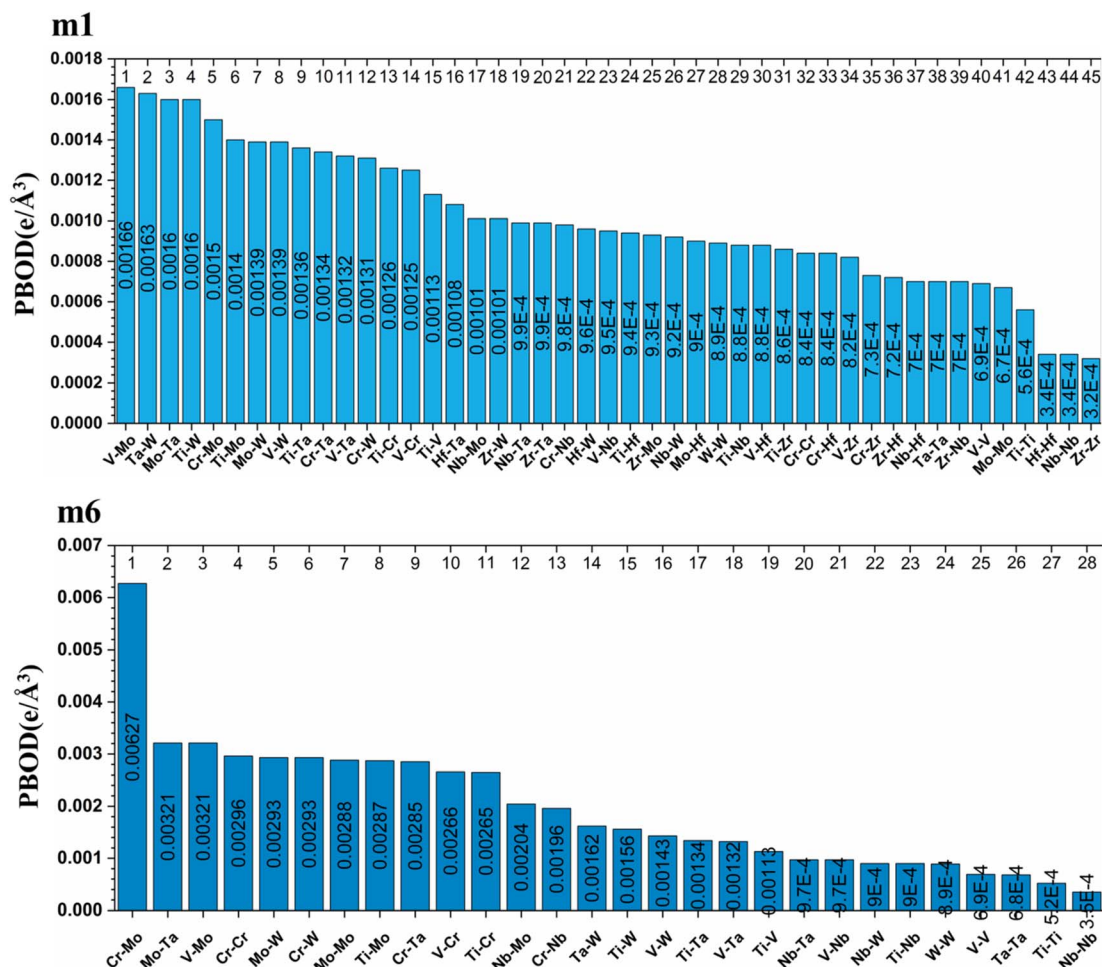
Fig. 8 Distribution of the PBOD in m1 and m6 RHEAs models as is displayed in bar charts.

elements. Cr and Mo along with V elements have the smallest atomic radius whereas Zr and Hf have the largest atomic radius (see Table S2†). Ti is the lightest element among these nine refractory elements. Manipulating the compositions of these five elements can lead to severe lattice distortion (or less lattice distortion), leading to extreme changes in the properties of these six RHEAs. In addition, Mo and Cr have BCC structure and the highest elemental VEC (VEC = 6), whereas Ti, Zr, and Hf have HCP structure and the lowest elemental VEC (VEC = 4). Therefore, altering the atomic fraction of these elements significantly impacts the VEC value of these six RHEAs, leading

to notable changes in their mechanical properties. Considering these factors, the atomic fraction of the five elements were selected for adjustment. However, the specific values of the atoms fractions were chosen randomly. For example, increasing the compositions of Cr and Mo from 0.111 in m1 and m2 to 0.135 in m3 and reducing the compositions of Zr and Hf from 0.111 in m1 and m2 to 0.088 in m3 resulted in larger elastic constants, mechanical moduli, and hardness, whereas a noticeable reduce in lattice distortion (see Tables 7 and 8).

Hf is heavy element and reducing its composition leads to less lattice distortion in m3 (see Table 8). In m4, Ti composition

Table 7 The calculated elastic constants C_{ij} (GPa), bulk modulus (K), shear modulus (G), Young's modulus (E) in GPa, Poisson's ratio (η), Pugh's ratio (G/K), Vicker's hardness (H_V), machinability index (μ_M), and Cauchy pressure (CP), and total bond order density(TBOD) of various TiVCrZrNbMoHfTaW system

Model	C_{11}	C_{12}	C_{44}	K	G	E	η	G/K	H_V	H_V(S12)	μ_M	CP
m1	225.43	127.72	32.48	160.22	38.24	106.27	0.390	0.239	2.381	2.980	4.933	95.24
m2	228.01	126.22	34.46	160.09	40.29	111.51	0.384	0.252	2.624	3.269	4.646	91.76
m3	246.77	132.38	35.48	170.38	42.99	118.95	0.384	0.252	2.755	3.396	4.802	96.90
m4	223.29	124.98	38.75	157.72	42.60	117.24	0.376	0.270	2.958	3.662	4.070	86.23
m5	276.32	139.41	39.56	184.82	49.35	135.95	0.377	0.267	3.241	3.939	4.673	99.85
m6	345.93	148.40	50.35	213.68	66.17	179.94	0.360	0.310	4.720	5.569	4.244	98.05

Table 8 The FWHM of the two Gaussians peaks and their average as a measure for lattice distortion in six RHEAs models

#	Model	FWHM 1	FWHM 2	Sum.	Ave.
1	m1	0.25788	0.33363	0.59151	0.29576
2	m2	0.26008	0.30319	0.56327	0.28164
3	m3	0.25425	0.28274	0.53699	0.26850
4	m4	0.25177	0.32682	0.57859	0.28930
5	m5	0.21093	0.24131	0.45224	0.22612
6	m6	0.15054	0.16812	0.31866	0.15933

was increased from 0.111 to 0.1604; the compositions of Ta and W were increased from 0.111 to 0.116; the compositions of Cr, Zr, and Mo were increased from 0.111 to 0.115; while the compositions of V and Nb were reduced from 0.111 to 0.064 and 0.097 respectively. This caused an increase in lattice distortion and hardness while elastic constants (C_{11} and C_{12}) and bulk modulus reduced significantly in m4. Lattice distortion effect is going to be discussed in detail in the next section. From Table 7, C_{11} has significantly increased in m5 and m6 (276.3 GPa and 345.9 GPa, respectively) comparing to m1, m2, and m4 due to the increase of Cr and Mo content from 114 atoms in m1to 228 atoms in m5 and m6 models. Increasing the Cr and Mo compositions in this class of RHEAs could be the key factor in improving the yield strength. C_{44} determines the exact resistance against the shear deformation in the (100) plane. Possessing the highest C_{44} values, m5 and m6 exhibit the lowest shearability (less responsive to shear stress) amongst all studied solid solutions. Higher Cr and Mo content in m5 and m6 results in significantly increased elastic constants compared to m1 and m4. This suggests that m5 and m6 experience lower elastic strains under stress. Increasing Ti content from 114 atoms in m1 to 164 atoms in m4 led to a significant decrease in C_{11}. The calculated elastic constants in Table 7 satisfy the mechanical stability criteria of a cubic structure: $C_{44} > 0$, $C_{11} > |C_{12}|$, and $C_{11} + 2C_{12} > 0$.[100] This suggests that these alloys are expected to be mechanically stable.

We obtained the mechanical parameters: bulk modulus (K), Young's modulus (E), shear modulus (G), and Poisson's ratio (η) from elastic coefficient C_{ij} using Voigt–Reuss–Hill (VRH) approximation.[101,102] The compliance tensor S_{ij} ($S_{ij} = 1/C_{ij}$) was also employed in the calculation. These derived properties are presented in Table 7 and Fig. 9(a). Young's modulus measures the change in length. Bulk modulus determines the resistance to compressibility or change in volume under pressure and shear modulus measures the resistance against shear distortion. A significant increase of K, E and G moduli in m5 and m6 due to the increased compositions of Cr and Mo. Fig. 9(a) show the model m6 has the highest values for K, G, and E, m4 exhibits the lowest values for K, and m1 exhibits the lowest values for both G and E. All these six RHEAs models are considered incompressible due to the high values of bulk modulus (higher than 40 GPa). It is crucial to determine the machinability index (μ_M) to assess the applications in different materials. Machinability is the ease with which the materials can be machined at a low cost. Eqn (S10) in the ESI† is used to calculate μ_M. Table 7 shows minimal variation in μ_M across the different compositions of the refractory elements in these six models. Pugh's modulus ratio,[102,103] defined as the ratio of shear modulus (G) to the bulk modulus (K), can sometimes be used to predict the brittle or ductile behavior of a material. Materials with G/K larger than 0.571 tend to be brittle while those with less than 0.571 tend to be ductile.[103,104] Based on Pugh's modulus ratio values in Table 7, all the six RHEAs models show a strong ductile behaviour.

Pettifor proposed the Cauchy pressure (CP)[105] as the difference between the elastic constants C_{12} and C_{44}: CP = $C_{12} - C_{44}$. A negative CP indicates dominance of covalent bonding and likely to have brittleness, while a positive CP indicates dominance of metallic bonding[106] and likely to have ductility.[107,108] As shown in Table 7, the metallic bonding is dominant in all six models. Vicker's hardness (H_V)[109,110] has been calculated using eqn (S11) based on the elastic constants.[111–113] The calculated values of H_V for the six RHEAs solid solutions are listed in Table 7. With these values of H_V, these RHEAs solid solutions cannot
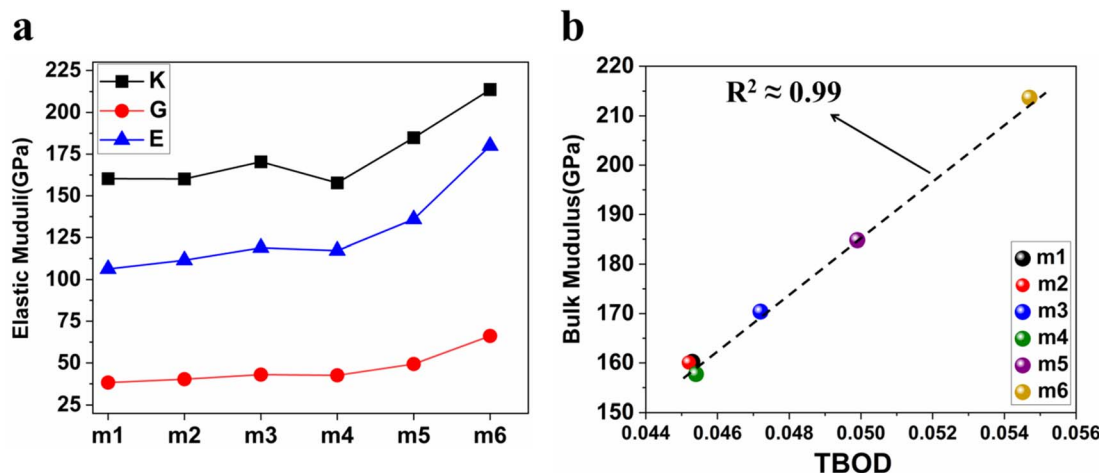

Fig. 9 (a) The distribution of Young's modulus (E), bulk modulus (K), and shear modulus (G) for the 6 BCC RHEAs. (b) Illustrates the relationship between total bond order density (TBOD) and the bulk modulus (K) for the same set of 6 BCC RHEAs.
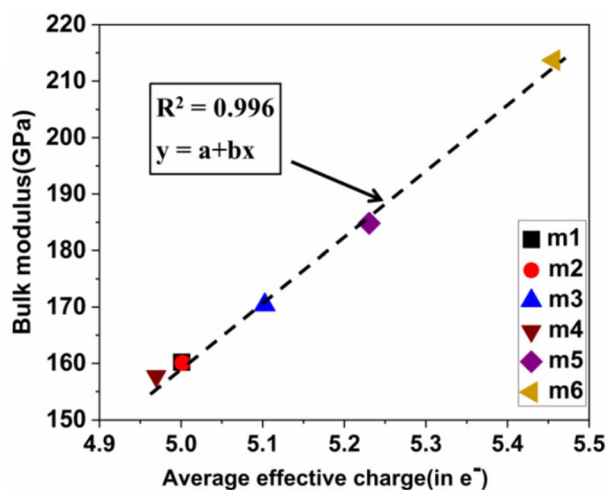
Fig. 10 Calculated Q_{ave}^* *versus* bulk modulus K for the set of 6 BCC RHEAs. The dashed line denotes linear fit.

be considered as super hard materials. Another formula (S12)† was used to estimate H_V. These values of H_V are presented in the column eleven of Table 7. Formula (S12)† shows that these six models have higher H_V than when using formula (S11),† however, m6 still has the highest H_V amongst other models. A relationship between the mechanical properties and the electronic structure is explored. For example, Fig. 9(b) illustrates the correlation between TBOD and bulk modulus. This correlation exhibits a closer-to-linear nature with their coefficient of determination (R^2) equaling 0.99. This observation suggests the potential future prediction of bulk modulus based on TBOD. Fig. 10 illustrates the positive correlation between bulk modulus (K) and Q_{ave}^* with their coefficient of determination (R^2) equaling 0.996, and this refers to the extreme importance of Q_{ave}^* in designing HEAs.

Finally, it is worthwhile to investigate the effects of incorporating HCP structures (the favored structure for Ti, Zr, and Hf under standard conditions) in these six RHEAs.

The type of crystalline structure (HCP or BCC) have a huge effect on the values of bulk modulus (K), Young's modulus (E), and VEC of RHEAs. K or E is one of the intrinsic nature of materials. Hf has HCP structure, while Ti and Zr can have either HCP or BCC structure. Therefore, changing the composition of these three elements may result in a dramatic change on the values of K, E, and VEC. K and E are also strongly correlated with VEC. Increasing proportion of HCP structures (Ti and Zr) while reducing BCC structure (V) within a BCC structure of a RHEA stabilize HCP structure (and destabilize BCC structure). This results in a significant decrease of K, E, and VEC values, as observed in m4 (see Tables 2 and 7). While reducing the composition of Zr and Hf and increasing the composition of Cr and Mo (BCC structures) stabilize BCC structure and result in larger K, E, and VEC values as observed in m3 and m5 (see Tables 2 and 7). The same trend can be seen in m6. We conclude that the type of crystalline structure (HCP or BCC) plays an important role in K, E, and VEC values of these RHEAs.

3.5. Lattice distortion

Lattice distortion (LD) has a huge effect on the properties of HEAs[2] such as mechanical and thermal properties. More large elastic-strains could be induced by LD which in return may hinder the dislocation motion during deformation.[114] LD can significantly modify the dislocation core structure[115] which suggests a correlation between LD and strength/ductility in HEAs.[116] Quantifying LD in HEAs is difficult beyond the simple geometric parameters. It is also difficult to capture LD in experiments. However, LD can be obtained from the BO *vs.* BL data. It is difficult to provide a precise description for LD due to the lack of a basic reference for the undistorted lattice in HEAs. In this work, LD is obtained by plotting the histogram distribution of BL data of interatomic pairs in Fig. 11 for m1 and m6, and Fig. S8† for all RHEAs models. Basically, the two peaks in these figures belong to the first nearest neighbor (NN) and second nearest neighbor (SNN) interatomic pairs.
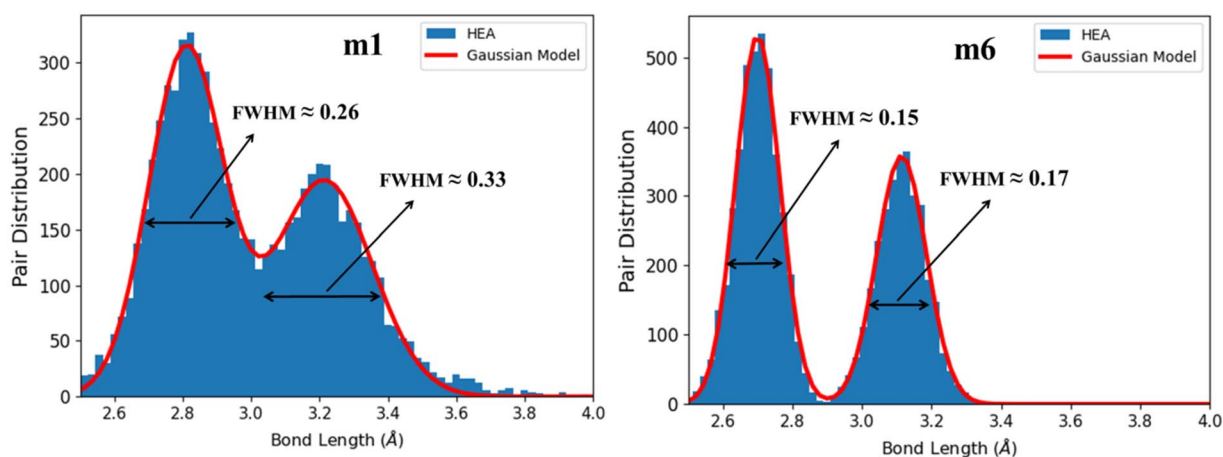

Fig. 11 Lattice distortion (LD) in m1 and m6 RHEAs models. FWHM of the Gaussian curve fitted to the histogram distribution of the bimodal peaks. The two peaks denote the NN and SNN.

These data were fitted with two Gaussians exhibiting a bimodal distributions for the NN and SNN. The full width at half maximum (FWHM) values obtained from BO values are presented in Table 8. Notable peaks show the structure integrity, whereas the pair distribution between the peaks denotes structure's LD. The larger the two FWHM and their sum, the greater the LD. From Table 8, m1 model displays the higher degree of LD while m6 displays the lower degree of LD. This indicates equimolar atomic ratios for these nine elements may result in larger LD. Increasing the compositions of Cr and Mo from 0.111 in m1 and m2 to 0.223 in m6 and reducing the compositions of Zr and Hf from 0.111 in m1 and m2 to zero in m6 resulted in much less LD and much higher elastic properties and hardness. This feature can be used to guide future experimental and computational works. In literature, the correlation between LD and ductility of HEAs is ambiguous and misleading. LD may be used as a parameter to predict the ductility of arbitrary HEAs. LD can significantly modify the dislocation core structure. Large elastic-strains could be induced by large LD which in return hinders the dislocation motion during the deformation[99,114] affecting the ductility and strength of HEAs.[117–121] Several parameters are used to predict the ductility of RHEAs: Cauchy pressure, Pugh's ratio, and Poisson's ratio. Small Pugh's ratio and large Poisson's ratio indicate ductile behavior. In Fig S9,† Pugh's ratio decreases with increase of LD and Poisson's ratio increases with increase in LD, indicating a strong correlation between LD and ductility of these six RHEAs models.

LD has a huge effect on many crucial properties including mixing entropies, electrical transport, and mechanical properties of HEAs as many previous studies have reported.[23,26,122] Thus, it is significant to explore the effect of LD on mechanical properties for these six RHEAs models by plotting LD (average value of FWHM1 and FWHM2 from Table 8) versus bulk (K) and shear (G) moduli in Fig. S10,† LD versus Young's modulus (E) and Vicker's hardness (H_V) in Fig. S11,† and LD versus elastic constants (C_{11} and C_{44}) in Fig. S12.† Fig. S10, S11, and S12† show that K, G, E, H_V, C_{11}, and C_{44} decrease with increase of LD, showing that LD generally decreases the strength and hardness of these six RHEAs models. The present results uncover that LD obviously lessen the elastic properties, which is consistent with some of previous findings.[27,123,124] This effect may be universal phenomenon irrespective of lattice structure of RHEAs. Fig. S11(b)† shows that LD and H_V are inversely correlated with a small deviation in m4.

3.6. Thermal properties

It is crucial to calculate thermal properties such as Debye temperature and thermal conductivity of the six RHEAs models since they determine the thermoelectric (TE) performance. TE performance of materials is the ability to convert heat into electricity under a temperature gradient. TE technology could be one of the green solutions to mitigate the energy and environmental crisis via reducing the pollution resulting from using fossil fuels.[125] TE performance is determined by so called figure of merit (ZT) which is given as: $ZT = S^2\sigma T/\kappa$, where σ is the electrical conductivity, S is the Seebeck coefficient, T is the absolute temperature, and κ is the thermal conductivity.

Due to the significant reduced κ, HEAs could be promising TE materials. The severe LD and chemical disorder may result in a significant phonon scattering and reduced κ. Several thermal characteristics could be described by the value of Debye temperature (Θ_D), such as the specific heat, thermal conductivity (κ), melting temperature, and the nature of bonding. In this work, we used Anderson's method (shown in eqn (S13) in the ESI†) to calculate Θ_D. The average sound velocity (ν_m), transverse (shear) sound velocity (ν_s), and the longitudinal sound velocity (ν_l) were calculated using eqn (S14)–(S16)† respectively.

The calculated ν_s, ν_l, ν_m, and Θ_D for the six RHEAs models are listed in Table 9. m6 has the highest Θ_D and ν_m, while m1 has the smallest ν_m and Θ_D. This may indicate that m1 has the weakest bond strength and lowest thermal conductivity whereas m6 has the strongest bonds and higher thermal conductivity. This result suggests a possible link between TBOD and these properties as m6 has the highest TBOD (see Table 6) and is a more cohesive structure. Low Θ_D is usually associated with low melting temperature while materials with high Θ_D tend to have stronger interatomic bonding and higher melting temperature.[48,126]

The performance of heat transfer through a material can be determined by the thermal conductivity (κ).[127] Calculating minimum thermal conductivity (κ_{min}) and lattice thermal conductivity (κ_L) in HEAs is important to verify the TE performance. In this work, we used Clarke's model[128] (see eqn (S17)†), Cahill's model[129] (see eqn (S18)†), Slack's model[130] (see eqn (S19)†), and mixed model (see eqn (S23)†) to obtain an estimation for κ_{min} and κ_L of the six RHEAs models 300 K and they are listed in Table 10. m1 has the lowest κ_{min} and κ_L according to Clarke's, Cahill's, and Slack's models while m6 has the highest κ_{min} and κ_L. From Table 10, m1 has the smallest value of ν_s. The significantly dampened transverse phonon modes (ν_s)

Table 9 The theoretical density (ρ), the calculated sound velocity (longitudinal ν_l, transverse ν_s, and average ν_m), Debye temperature Θ_D, and velocity estimated from Young's modulus (ν_E) of various TiVCrZrNbMoHfTaW system

Model	ρ (Kg m^{-3})	ν_s (m s^{-1})	ν_l (m s^{-1})	ν_m (m s^{-1})	Θ_D (K)	ν_E (m s^{-1})
m1	10 571.57	1901.907	4469.759	2149.883	249.03	3170.558
m2	10 568.52	1952.502	4497.870	2205.391	255.44	3248.252
m3	10 553.26	2018.322	4645.027	2279.650	266.27	3357.291
m4	10 483.81	2015.790	4523.498	2274.441	262.84	3344.093
m5	10 516.87	2166.209	4881.628	2444.596	288.85	3595.394
m6	10 417.72	2520.254	5383.319	2837.257	341.99	4156.020

Table 10 The calculated minimum thermal (κ_{min}) and lattice thermal (κ_L) conductivities (W·m^{-1} K^{-1}) at 300 K, Grüneisen parameter (γ_a), melting temperature (T_{melt}), and thermal expansion coefficient (α) of various TiVCrZrNbMoHfTaW system

Model	Clarke model κ_{min} (W m^{-1} K^{-1})	Cahill model κ_{min} (W m^{-1} K^{-1})	Slack model κ_L (W m^{-1} K^{-1})	Mixed model κ_L (W m^{-1} K^{-1})	γ_α	T_{melt} (K)	α ($\times 10^{-5}$)
m1	0.5765	0.5367	0.4641	0.6636	2.506	1885.29	4.184
m2	0.5905	0.5432	0.5253	0.7388	2.447	1900.54	3.971
m3	0.6207	0.5707	0.5807	0.8044	2.444	2011.41	3.722
m4	0.6052	0.5482	0.6104	0.8439	2.368	1872.64	3.756
m5	0.6802	0.6177	0.7521	1.0070	2.381	2186.05	3.242
m6	0.8183	0.7208	1.3466	1.6919	2.214	2597.45	2.418

may strengthen the scattering of phonons[131] which in return results in a reduced lattice thermal conductivity (κ_L).

The Grüneisen parameter (γ_α) describes the bond anharmonicity and the nature of the interatomic interaction inside a material.[132] Large value of γ_α indicates strong anharmonic vibrations of atoms or molecules, and thus higher phonon scattering and lower κ_L. Formula (S21)† was used to calculate γ_α values and they are summarized in Table 10. With the highest γ_α, m1 is the lowest influenced under high temperature (depressed and temperature-independent lattice thermal conductivity) whereas m6 with lowest γ_α is the highest influenced under high temperature (higher and temperature-dependent lattice thermal conductivity). A higher Θ_D may indicate a higher κ_L and *vice versa* according to Callaway–Debye theoretical model.[133] Fig. S13(a)† shows that Θ_D is positively correlated (close-linear) with κ_L for the six RHEAs models and in agreement with Callaway–Debye model.

We also calculated melting temperature (T_{melt}) using formula (S24) in the ESI.† T_{melt} is an important parameter in high temperature applications. T_{melt} is usually correlated to Θ_D and κ_L. The calculated T_{melt} for the six RHEAs models is presented in Table 10. As expected, m6 has the highest T_{melt} whereas m4 has the lowest T_{melt}. The tendency of a material to change the shape, volume, and density in response to a change in temperature is described by thermal expansion coefficient (α). α for the six RHEAs models can be estimated from the formula (S25).† Table 10 shows that m1 has the largest α whereas m6 has the smallest α.

The random distribution of mismatch of atomic size in HEAs leads to a severe LD. Thus, LD should have a huge impact on thermal properties.[24,134,135] For example, higher LD causes stronger anharmonic vibrations (higher γ_α) (see Fig. S13(b)†) and this leads to higher phonon scattering and lower κ_L. According to this criterion, we plotted LD (average value of FWHM1 and FWHM2 from Table 8) *versus* Θ_D in Fig. S14(a)† and noticed that with the increase in LD, Θ_D significantly decreases. The same exact trend was noticed in Fig. S14(b) and S15(a).† With the increase in LD, ν_s and κ_L significantly decrease. This shows that LD strongly affects the thermal transport process. Small deviation could be noticed for m4. Strong anharmonic vibrations (high γ_α) indicates higher phonon scattering and lower κ_L, and this trend can be seen in Fig. S15(b).† With the increase in γ_α, κ_L significantly decreases.

4 Conclusion

In current study, electronic structure, bonding, mechanical, lattice distortion, and thermal properties of six BCC refractory-based HEAs (or RHEAs): TiVCrZrNbMoHfTaW(m1), TiVCrZrNbMoHfTaW(m2),Ti$_{114}$V$_{114}$Cr$_{138}$Zr$_{90}$Nb$_{114}$Mo$_{138}$Hf$_{90}$-Ta$_{113}$W$_{113}$(m3), Ti$_{164}$V$_{65}$Cr$_{118}$Zr$_{118}$Nb$_{99}$Mo$_{118}$Hf$_{104}$Ta$_{119}$W$_{119}$(m4), Ti$_{114}$V$_{114}$Cr$_{171}$Zr$_{57}$Nb$_{114}$Mo$_{171}$Hf$_{57}$Ta$_{113}$W$_{113}$(m5), and Ti$_{114}$V$_{114}$Cr$_{228}$Nb$_{114}$Mo$_{228}$Ta$_{113}$W$_{113}$(m6) were investigated *via* first-principles calculations. Phase stability of these six RHEAs has been tested *via* calculating thermodynamic parameters and other parameters. Random solid solution model (RSSM) was used for alloying these six RHEAs models with large super-cells of 1024 atoms each.

The effect of total bond order density (TBOD) as a valuable parameter in understanding the bonding characteristics of RHEAs is highlighted. The average partial charge (Q_{av}^*) for each model was calculated. It is shown that TBOD and Q_{av}^* are positively correlated with the mechanical properties, especially with bulk modulus. Based on our calculations, all these six RHEAs models are mechanically stable. m5 and m6 have the largest Young's, bulk, and shear moduli, whereas m1 and m2 have the lowest Young's, bulk, and shear moduli. Reducing the composition of Hf element from 114 atoms into 57 atoms, and increasing the composition of Cr and Mo elements to 171 atoms each in m5 resulted in larger elastic moduli (Young's, bulk, and shear) compared with other models. Reducing the composition of Hf and Zr elements into zero and increasing the composition of Cr and Mo elements into 228 atoms each in m6 resulted in larger elastic moduli (even larger than m5) and large elastic constants (C_{11} and C_{44}) compared with other models indicating higher hardness with higher fracture toughness and melting temperature. Larger elastic moduli indicates higher difficulty to compress and elongate.

Different atomic configurations can result in a significant different property. For example, the total density of states of m2 and partial density of states (PDOS) at Fermi energy of most elements in m2 lowered compared to m1 indicating that m2 is more stable than m1(see Tables 3 and 4). Elastic constants (C_{11} and C_{44}), shear and Young's moduli, Pugh's ratio, and Vicker's hardness increased in m2 comparing to m1. This indicates that mechanical properties can be improved *via* changing the atomic configurations in HEAs. The atomic configuration has also an effect on lattice distortion and thermal properties. Different atomic configurations can cause either higher or lower lattice

distortion which in return results in different mechanical and thermal properties. Lattice thermal conductivity increased in m2 comparing to m1, whereas lattice distortion decreased (see Tables 7, 8, and 10). If the atomic configuration can influence the lattice distortion, it indeed influences the dislocation dynamics and further in mechanical properties of HEAs. This suggests that manipulating the atomic configuration would be an effective strategy to enhance the mechanical properties. Similarly, changing atomic configurations can be carried out for each model from m3 to m6 to produce other new different models with different physical properties. However, this process would be very computationally expensive in the current study.

Controlling the VEC value is a key factor in achieving either high or low Young's modulus (E) and bulk modulus (K). Both E and K are positively correlated to VEC as shown in Fig. S16.† This strongly suggests that increasing the composition of elements with low VEC value such as Ti, Zr, and Hf lowers the VEC of the RHEA, thereby reducing E and K (as observed in m4). Conversely, decreasing the composition of Ti, Zr, and Hf while increasing the proportion of elements with high VEC values, such as Cr, Mo, and W, raises the VEC of the RHEA, resulting in significantly higher E and K (as seen in m5 and m6). VEC values can also control melting point (T_m) (see Table 2) of RHEAs. Fig. S17† shows that the correlation between T_m and VEC of the six RHEAs is almost positively linear with ($R^2 \approx 0.995$). VEC along with the type of crystalline structure can be used to manipulate the mechanical and thermal properties of RHEAs. This analysis can open new avenues for the designing more RHEAs for multiple applications.

Thermal properties and TE performance of these six RHEAs were investigated. m1 and m2 have the smallest velocity of a sound ($vs.$, v_l, v_m), Θ_D, and κ_L, whereas m5 and m6 have the largest $vs.$, v_l, v_m, Θ_D, and κ_L. The velocity of a sound is usually determined by two factors: the elastic properties and density (ρ), and the relationship is described by the following equation:

$$v = \sqrt{\frac{C_{ij}}{\rho}} \tag{14}$$

Reducing the composition of Hf and Zr elements to zero in m6 affected thermal properties significantly. m6 has the lowest density among other models. Larger Θ_D in m5 and m6 indicates stronger interatomic bonding and as a result, sound waves travel faster in these two models. The larger Θ_D positively correlates with TBOD. High sound velocities or high phonon speeds indicates larger κ_L. This feature makes the m5 and m6 models less applicable for TE applications, whereas m1 and m2 are more applicable for TE applications. These six RHEAs models were investigated for their lattice distortion (LD). m1, m2, and m4 have the highest LD while models m5 and m6 have the lowest LD. We showed that LD is correlated to the ductility of these six RHEAs models. LD is correlated with lattice thermal conductivity (κ_L). A high LD indicates higher phonon scattering and thus low κ_L, while a small LD indicates higher κ_L. This new finding from our current calculations could be facilitated to design new RHEAs for multiple uses. The promising current

results inspire us to do more research in this direction for more complex refractory-based high-entropy materials. We believe our results can be facilitated to design new high-entropy materials with wider applications.

Data availability

The authors declare that the main data supporting the findings of this study are available within the article and its ESI files.† Any additional information, such as codes used in this study, is available either in the ESI† or upon request *via* contacting the first author at: sahibhasan81@gmail.com.

Author contributions

Wai-Yim Ching (W. C.) conceived and directed the project. W. C., Saro San (S. S.), and Sahib Hasan (S. H.) performed the calculations. S. S. and S. H. made all figures. S. H., Puja Adhikari, and W. C. drafted the paper. All authors participated in the discussion and interpretation of the results. All authors edited and proofread the final manuscript.

Conflicts of interest

The authors declare no competing or conflicts of interests.

Acknowledgements

References

1 C. J. Tong, et al., Mechanical performance of the AlxCoCrCuFeNi high-entropy alloy system with multiprincipal elements, *Metall. Mater. Trans. A*, 2005, **36**, 1263–1271.

2 C. Lee, et al., Lattice distortion in a strong and ductile refractory high-entropy alloy, *Acta Mater.*, 2018, **160**, 158–172.

3 Y. Shi, et al., Corrosion of Al xCoCrFeNi high-entropy alloys: Al-content and potential scan-rate dependent pitting behavior, *Corros. Sci.*, 2017, **119**, 33–45.

4 O. N. Senkov, G. B. Wilks, D. B. Miracle, C. P. Chuang and P. K. Liaw, Refractory high-entropy alloys, *Intermetallics*, 2010, **18**, 1758–1765.

5 W. R. Wang, W. L. Wang and J. W. Yeh, Phases, microstructure and mechanical properties of AlxCoCrFeNi high-entropy alloys at elevated temperatures, *J. Alloys Compd.*, 2014, **589**, 143–152.

6 Y. L. Chou, J. W. Yeh and H. C. Shih, Effect of Inhibitors on the Critical Pitting Temperature of the High-Entropy Alloy

Co1.5CrFeNi1.5Ti0.5Mo0.1, *J. Electrochem. Soc.*, 2011, **158**, C246.

7 Y. F. Kao, T. D. Lee, S. K. Chen and Y. S. Chang, Electrochemical passive properties of AlxCoCrFeNi (x = 0, 0.25, 0.50, 1.00) alloys in sulfuric acids, *Corros. Sci.*, 2010, **52**, 1026–1034.

8 Y. Geng, et al., Remarkable Wear Resistance in a Complex Concentrated Alloy with Nanohierarchical Architecture and Composition Undulation, *Research*, 2023, **6**, 1–14.

9 D. Bérardan, S. Franger, D. Dragoe, A. K. Meena and N. Dragoe, Colossal dielectric constant in high entropy oxides, *Phys. Status Solidi Rapid Res. Lett.*, 2016, **10**, 328–333.

10 K. Stolze, J. Tao, F. O. Von Rohr, T. Kong and R. J. Cava, Sc-Zr-Nb-Rh-Pd and Sc-Zr-Nb-Ta-Rh-Pd High-Entropy Alloy Superconductors on a CsCl-Type Lattice, *Chem. Mater.*, 2018, **30**, 906–914.

11 M. H. Tsai, Physical properties of high entropy alloys, *Entropy*, 2013, **15**, 5338–5345.

12 J. W. Yeh, et al., Nanostructured high-entropy alloys with multiple principal elements: Novel alloy design concepts and outcomes, *Adv. Eng. Mater.*, 2004, **6**, 299–303.

13 D. B. Miracle and O. N. Senkov, A critical review of high entropy alloys and related concepts, *Acta Mater.*, 2017, **122**, 448–511.

14 Z. Li, S. Zhao, R. O. Ritchie and M. A. Meyers, Mechanical properties of high-entropy alloys with emphasis on face-centered cubic alloys, *Prog. Mater. Sci.*, 2019, **102**, 296–345.

15 S. Gorsse, J. P. Couzinié and D. B. Miracle, From high-entropy alloys to complex concentrated alloys, *Compt. Rendus Phys.*, 2018, **19**, 721–736.

16 O. N. Senkov, D. B. Miracle, K. J. Chaput and J. P. Couzinie, Development and exploration of refractory high entropy alloys - A review, *J. Mater. Res.*, 2018, **33**, 3092–3128.

17 J. Han, B. Su, J. Meng, A. Zhang and Y. Wu, Microstructure and composition evolution of a fused slurry silicide coating on MoNbTaTiW refractory high-entropy alloy in high-temperature oxidation environment, *Materials*, 2020, **13**, 3592.

18 A. Ostovari Moghaddam, A. Cabot and E. A. Trofimov, Does the pathway for development of next generation nuclear materials straightly go through high-entropy materials?, *Int. J. Refract. Met. Hard Mater.*, 2021, **97**, 105504.

19 J. W. Yeh, Alloy design strategies and future trends in high-entropy alloys, *Jom*, 2013, **65**, 1759–1771.

20 D. Juliusz, Z. Marek, W. Kucza, G. C. slak, K. Berent, T. Czeppe and M. D. Tadeusz Kulik, Demystifying the sluggish diffusion effect in high entropy alloys, *J. Alloys Compd.*, 2019, **783**, 193–207.

21 J.-W. Yeh, C. Shou-Yi, H. Yu-Der and S.-J. L. Swe-Kai Chen, Anomalous decrease in X-ray diffraction intensities of Cu–Ni–Al–Co–Cr–Fe–Si alloy systems with multi-principal elements, *Mater. Chem. Phys.*, 2007, **103**, 41–46.

22 B. Jiang, et al., High-entropy-stabilized chalcogenides with high thermoelectric performance, *Science*, 2021, **371**, 830–834.

23 H. Song, et al., Local lattice distortion in high-entropy alloys, *Phys. Rev. Mater.*, 2017, **1**, 1–8.

24 C. M. Rost, et al., Electron and phonon thermal conductivity in high entropy carbides with variable carbon content, *Acta Mater.*, 2020, **196**, 231–239.

25 K. Y. Tsai, M. H. Tsai and J. W. Yeh, Sluggish diffusion in Co-Cr-Fe-Mn-Ni high-entropy alloys, *Acta Mater.*, 2013, **61**, 4887–4897.

26 S. S. Sohn, et al., Ultrastrong Medium-Entropy Single-Phase Alloys Designed via Severe Lattice Distortion, *Adv. Mater.*, 2019, **31**, 1–8.

27 B. Feng and M. Widom, Elastic stability and lattice distortion of refractory high entropy alloys, *Mater. Chem. Phys.*, 2018, **210**, 309–314.

28 L. Xiang, Microstructure and Mechanical Properties of TaNbVTiAlx Refractory High-Entropy Alloys, *Entropy*, 2020, **22**, 282.

29 Y. Zhang, et al., Microstructures and properties of high-entropy alloys, *Prog. Mater. Sci.*, 2014, **61**, 1–93.

30 O. N. Senkov, G. B. Wilks, J. M. Scott and D. B. Miracle, Mechanical properties of Nb25Mo25Ta 25W25 and V20Nb20Mo 20Ta20W20 refractory high entropy alloys, *Intermetallics*, 2011, **19**, 698–706.

31 O. N. Senkov, J. M. Scott, S. V. Senkova, D. B. Miracle and C. F. Woodward, Microstructure and room temperature properties of a high-entropy TaNbHfZrTi alloy, *J. Alloys Compd.*, 2011, **509**, 6043–6048.

32 S. K. Bachani, C. J. Wang, B. S. Lou, L. C. Chang and J. W. Lee, Microstructural characterization, mechanical property and corrosion behavior of VNbMoTaWAl refractory high entropy alloy coatings: Effect of Al content, *Surf. Coating. Technol.*, 2020, **403**, 126351.

33 O. N. Senkov, S. Gorsse and D. B. Miracle, High temperature strength of refractory complex concentrated alloys, *Acta Mater.*, 2019, **175**, 394–405.

34 E. P. George, W. A. Curtin and C. C. Tasan, High entropy alloys: A focused review of mechanical properties and deformation mechanisms, *Acta Mater.*, 2020, **188**, 435–474.

35 Y. Zou, S. Maiti, W. Steurer and R. Spolenak, Size-dependent plasticity in an Nb25Mo25Ta25W25 refractory high-entropy alloy ScienceDirect Size-dependent plasticity in an Nb 25 Mo 25 Ta 25 W 25 refractory high-entropy alloy, *Acta Mater.*, 2017, **65**, 85–97.

36 Y. Zou, H. Ma and R. Spolenak, Ultrastrong ductile and stable high-entropy alloys at small scales, *Nat. Commun.*, 2015, **6**, 7748.

37 S. Y. Chen, et al., Peierls barrier characteristic and anomalous strain hardening provoked by dynamic-strain-aging strengthening in a body-centered-cubic high-entropy alloy, *Mater. Res. Lett.*, 2019, **7**, 475–481.

38 O. N. Senkov, J. M. Scott, S. V. Senkova, F. Meisenkothen, D. B. Miracle and C. F. Woodward, Microstructure and elevated temperature properties of a refractory TaNbHfZrTi alloy, *J. Mater. Sci.*, 2012, **47**, 4062–4074.

39 Q. T. Song and J. Xu, TiZrNbTa)90Mo10 high-entropy alloy: Electrochemical behavior and passive film characterization under exposure to Ringer's solution, *Corros. Sci.*, 2020, **167**, 108513.

40 J. Li, X. Yang, R. Zhu and Y. Zhang, Corrosion and Serration Behaviors of TiZr0.5NbCr0.5VxMoy High Entropy Alloys in Aqueous Environments, *Metals*, 2014, **4**, 597–608.

41 Q. Zhou, et al., Corrosion behavior of Hf0.5Nb0.5Ta0.5Ti1.5Zr refractory high-entropy in aqueous chloride solutions, *Electrochem. Commun.*, 2019, **98**, 63–68.

42 S. P. Wang and J. Xu, TiZrNbTaMo high-entropy alloy designed for orthopedic implants: As-cast microstructure and mechanical properties, *Mater. Sci. Eng. C*, 2017, **73**, 80–89.

43 N. Y. Yurchenko, N. D. Stepanov, S. V. Zherebtsov, M. A. Tikhonovsky and G. A. Salishchev, Structure and mechanical properties of B2 ordered refractory AlNbTiVZrx (x = 0–1.5) high-entropy alloys, *Mater. Sci. Eng., A*, 2017, **704**, 82–90.

44 Z. D. Han, et al., Effect of Ti additions on mechanical properties of NbMoTaW and VNbMoTaW refractory high entropy alloys, *Intermetallics*, 2017, **84**, 153–157.

45 G. Kresse, Efficient iterative schemes for ab initio total-energy calculations using a plane-wave basis se, *Phys. Rev. B*, 1996, **54**, 11169.

46 J. P. Perdew, K. Burke and M. Ernzerhof, Generalized gradient approximation made simple, *Phys. Rev. Lett.*, 1996, **77**, 3865–3868.

47 H. J. Monkhorst and J. D. Pack, Special points for Brillonin-zone integrations, *Phys. Rev. B*, 1976, **13**, 5188.

48 A. Yang, L. Bao, M. Peng and Y. Duan, Explorations of elastic anisotropies and thermal properties of the hexagonal TMSi2 (TM = Cr, Mo, W) silicides from first-principles calculations, *Mater. Today Commun.*, 2021, **27**, 102474.

49 A. J. Wang, et al., Structural and elastic properties of cubic and hexagonal TiN and AlN from first-principles calculations, *Comput. Mater. Sci.*, 2010, **48**, 705–709.

50 A. Reuss, Berechnung der Fließgrenze von Mischkristallen auf Grund der Plastizitätsbedingung für Einkristalle, *J. Appl. Math. Mech.*, 1929, **9**, 49–58.

51 R. HILL, The Elastic Behaviour of a Crystalline Aggregate, *Proc. Phys. Soc.*, 1952, **65**(5), 349.

52 Y. Mo, P. Rulis and W. Y. Ching, Electronic structure and optical conductivities of 20 MAX-phase compounds, *Phys. Rev. B Condens. Matter*, 2012, **86**, 1–10.

53 S. Hasan, P. Adhikari, K. Baral and W. Y. Ching, Conspicuous interatomic bonding in chalcogenide crystals and implications on electronic, optical, and elastic properties, *AIP Adv.*, 2020, **10**, 7.

54 S. Hasan, K. Baral, N. Li and W. Y. Ching, Structural and physical properties of 99 complex bulk chalcogenides crystals using first-principles calculations, *Sci. Rep.*, 2021, **11**, 1–18.

55 C. Dharmawardhana, M. Bakare, A. Misra, W. Y. Ching and J. Bullard, Nature of Interatomic Bonding in Controlling the Mechanical Properties of Calcium Silicate Hydrates, *J. Am. Ceram. Soc.*, 2016, **99**, 2120–2130.

56 L. Poudel, C. Tamerler, A. Misra and W. Y. Ching, Atomic-Scale Quantification of Interfacial Binding between Peptides and Inorganic Crystals: The Case of Calcium Carbonate Binding Peptide on Aragonite, *J. Phys. Chem. C*, 2017, **121**, 28354–28363.

57 S. San, N. Li, Y. Tao, W. Zhang and W. Y. Ching, Understanding the atomic and electronic origin of mechanical property in thaumasite and ettringite mineral crystals, *J. Am. Ceram. Soc.*, 2018, **101**, 5177–5187.

58 S. Hasan, S. San, K. Baral, N. Li, P. Rulis and W. Y. Ching, First-principles calculations of thermoelectric transport properties of quaternary and ternary bulk chalcogenide crystals, *Materials*, 2022, **15**, 8.

59 S. Hasan, P. Rulis and W.-Y. Ching, First-Principles Calculations of the Structural, Electronic, Optical, and Mechanical Properties of 21 Pyrophosphate Crystals, *Crystals*, 2022, **12**, 8.

60 B. Hunca, C. Dharmawardhana, R. Sakidja and W. Y. Ching, Ab initio calculations of thermomechanical properties and electronic structure of vitreloy Z r41.2 T i13.8 C u12.5 N i10 B e22.5, *Phys. Rev. B*, 2016, **94**, 1–10.

61 W. Y. Ching, et al., First-principles study in an inter-granular glassy film model of silicon nitride, *J. Am. Ceram. Soc.*, 2018, **101**, 2673–2688.

62 S. Hasan, P. Adhikari, S. San, P. Rulis and W. Y. Ching, First-principles calculation of lattice distortion, electronic structure, and bonding properties of GeTe-based and PbSe-based high-entropy chalcogenides, *J. Appl. Phys.*, 2024, **135**, 085101.

63 S. H. Saro San, Designing Quaternary and Quinary Refractory-Based High-Entropy Alloys: Statistical Analysis of Their Lattice Distortion, Mechanical, and Thermal Properties, *Metals*, 2023, **13**, 1953.

64 L. Poudel, R. Twarock, N. F. Steinmetz, R. Podgornik and W. Y. Ching, Impact of Hydrogen Bonding in the Binding Site between Capsid Protein and MS2 Bacteriophage ssRNA, *J. Phys. Chem. B*, 2017, **121**, 6321–6330.

65 P. Adhikari, et al., Intra- And intermolecular atomic-scale interactions in the receptor binding domain of SARS-CoV-2 spike protein: Implication for ACE2 receptor binding, *Phys. Chem. Chem. Phys.*, 2020, **22**, 18272–18283.

66 R. S. Mulliken, Electronic population analysis on LCAO-MO molecular wave functions. I, *J. Chem. Phys.*, 1955, **23**, 1833–1840.

67 C. C. Dharmawardhana, A. Misra and W. Y. Ching, Quantum mechanical metric for internal cohesion in cement crystals, *Sci. Rep.*, 2014, **4**, 1–8.

68 W. Hume-Rothery, The Engel-Brewer theories of metals and alloys, *Prog. Mater. Sci.*, 1968, **13**, 229–265.

69 E. C. STONER, Atomic Theory Students of Metallurgy, *Nature*, 1947, **159**, 78–79.

70 Y. Zhang, Y. J. Zhou, J. P. Lin, G. L. Chen and P. K. Liaw, Solid-solution phase formation rules for multi-component alloys, *Adv. Eng. Mater.*, 2008, **10**, 534–538.

71 A. Takeuchi and A. Inoue, Classification of Bulk Metallic Glasses by Atomic Size Difference , Heat of Mixing and Period of Constituent Elements and Its Application to Characterization of the Main Alloying Element, *Mater. Trans.*, 2005, **46**, 2817–2829.

72 A. Raza, H. J. Ryu and S. H. Hong, Strength enhancement and density reduction by the addition of Al in CrFeMoV based high-entropy alloy fabricated through powder metallurgy, *Mater. Des.*, 2018, **157**, 97–104.

73 W. Guo, et al., Microstructures and mechanical properties of ductile NbTaTiV refractory high entropy alloy prepared by powder metallurgy, *J. Alloys Compd.*, 2019, **776**, 428–436.

74 X. Yang and Y. Zhang, Prediction of high-entropy stabilized solid-solution in multi-component alloys, *Mater. Chem. Phys.*, 2012, **132**, 233–238.

75 O. N. Senkov and D. B. Miracle, Effect of the atomic size distribution on glass forming ability of amorphous metallic alloys, *Mater. Res. Bull.*, 2001, **36**, 2183–2198.

76 B. Chanda and J. Das, Composition Dependence on the Evolution of Nanoeutectic in CoCrFeNiNb x (0.45 ≤ x ≤ 0.65) High Entropy Alloys, *Adv. Eng. Mater.*, 2018, **20**, 0–9.

77 U. Bhandari, H. Ghadimi, C. Zhang, S. Yang and S. Guo, Predicting Elastic Constants of Refractory Complex Concentrated Alloys Using Machine Learning Approach, *Materials*, 2022, **15**, 1–16.

78 S. Guo and C. T. Liu, Phase stability in high entropy alloys : Formation of solid-solution phase or amorphous phase, *Prog. Nat. Sci.:Mater. Int.*, 2011, **21**, 433–446.

79 S. Guo, C. Ng, J. Lu and C. T. Liu, Effect of valence electron concentration on stability of fcc or bcc phase in high entropy alloys, *J. Appl. Phys.*, 2011, **109**, 103505.

80 R. K. Nutor, et al., Phase Selection, Lattice Distortions, and Mechanical Properties in High-Entropy Alloys, *Adv. Eng. Mater.*, 2020, **22**, 1–36.

81 Y. Dong, Y. Lu, L. Jiang, T. Wang and T. Li, Effects of electronegativity on the stability of topologically close- packed phase in high entropy alloys, *Intermetallics*, 2014, **52**, 105–109.

82 M. G. Poletti and L. Battezzati, ScienceDirect Electronic and thermodynamic criteria for the occurrence of high entropy alloys in metallic systems, *Acta Mater.*, 2014, **75**, 297–306.

83 A. K. Singh, A geometrical parameter for the formation of disordered solid solutions in multi-component alloys, *Intermetallics*, 2014, **53**, 112–119.

84 F. Tian, L. K. Varga, N. Chen, J. Shen and L. Vitos, Intermetallics Empirical design of single phase high-entropy alloys with high hardness, *Intermetallics*, 2015, **58**, 1–6.

85 X. F. Wang, Y. Zhang, Y. Qiao and G. L. Chen, Novel microstructure and properties of multicomponent CoCrCuFeNiTi x alloys, *Intermetallics*, 2007, **15**, 357–362.

86 M.-R. Chen, Microstructure and Properties of Al0:5CoCrCuFeNiTix (x ¼ 0{2:0) High-Entropy Alloys, *Mater. Trans.*, 2006, **47**, 1395–1401.

87 Y. F. Ye, Q. Wang, J. Lu, C. T. Liu and Y. Yang, High-entropy alloy: challenges and prospects, *Mater. Today*, 2016, **19**, 349–362.

88 C. C Tung, J. W. Yeh, T. Shun, S. K. Chen, Y. S. Huang and H. C. Chen, On the elemental effect of AlCoCrCuFeNi high-entropy alloy system, *Mater. Lett.*, 2007, **61**(1), 1–5.

89 C. Tsai, J. Yeh & P. Lee Effect of the substitution of Co by Mn in Al-Cr-Cu-Fe-Co-Ni high-entropy alloys. (2006) doi:DOI: **10.3166/acsm.31.685-698**.

90 C. Li, Microstructure and properties of AlTiNiMnBx high entropy alloys, *Mater. Sci. Technol.*, 2008, 459.

91 Z. Wang, S. Guo & C. T. Liu Phase Selection in High-Entropy Alloys : From Nonequilibrium to Equilibrium*JOM* (2014) 1996 doi:DOI: **10.1007/s11837-014-0953-8**.

92 Y. Yuan, et al., Formation, structure and properties of biocompatible TiZrHfNbTa high-entropy alloys, *Mater. Res. Lett.*, 2019, **7**, 225–231.

93 X. Yang and Y. Zhang, Prediction of high-entropy stabilized solid-solution in multi-component alloys Prediction of high-entropy stabilized solid-solution in multi-component alloys, *Mater. Chem. Phys.*, 2017, **132**, 233–238.

94 S. Fang, X. Xiao, L. Xia, W. Li and Y. Dong, Relationship between the widths of supercooled liquid regions and bond parameters of Mg-based bulk metallic glasses, *J. Non-Cryst. Solids*, 2003, **321**(1–2), 120–125.

95 S. Fang, Z. Zhou, J. Zhang, M. Yao, F. Feng and D. Northwood, Two mathematical models for the hydrogen storage properties of AB2 type alloys, *J. Alloys Compd.*, 1999, **293–295**, 10–13.

96 L. Pauling and G. W. Wheland, The Nature of the Chemical Bond. V, *J. Chem. Phys.*, 1934, **2**, 482.

97 I. Toda-Caraballo and P. E. J. Rivera-Díaz-Del-Castillo, A criterion for the formation of high entropy alloys based on lattice distortion, *Intermetallics*, 2016, **71**, 76–87.

98 N. Yurchenko, N. Stepanov and G. Salishchev, Laves-phase formation criterion for high-entropy alloys, *Mater. Sci. Technol.*, 2016, **33**(1), 17–22.

99 P. Singh, et al., A ductility metric for refractory-based multi-principal-element alloys, *Acta Mater.*, 2023, **257**, 1–36.

100 F. Mouhat and F. X. Coudert, Necessary and sufficient elastic stability conditions in various crystal systems, *Phys. Rev. B Condens. Matter*, 2014, **90**, 0–3.

101 R. Hill, The elastic behaviour of a crystalline aggregate, *Proc. R. Soc. Edinb. Sect. A*, 1952, **65**, 349–354.

102 S. F. Pugh, Relations between the elastic moduli and the plastic properties of polycrystalline pure metals, *Philos. Mag. Ser. 7*, 1954, **45**(367), 823–843.

103 M. Ali, Md. Hossain, M. Rayhan, M. Hossain, M. R. Uddin, K. Ostrikov, A. Islam and S. Naqib, First-principles study of elastic, electronic, optical and thermoelectric properties of newly synthesized K2Cu2GeS4 chalcogenide, *J. Alloys Compd.*, 2019, **781**, 37–46.

104 D. Heciri, et al., Insight into the structural, elastic and electronic properties of tetragonal inter-alkali metal chalcogenides CsNaX (X=S, Se, and Te) from first-principles calculations, *Mater. Chem. Phys.*, 2019, **221**, 125–137.

105 D. G. Pettifor, Theoretical predictions of structure and related properties of intermetallics, *Mater. Sci. Technol.*, 1992, **8**, 345–349.

106 G. Surucu, M. Isik, A. Candan, X. Wang and H. H. Gullu, Investigation of structural, electronic, magnetic and lattice dynamical properties for XCoBi (X: Ti, Zr, Hf) Half-

Heusler compounds, *Phys. B Condens. Matter*, 2020, **587**, 412146.

107 L. Bao, D. Qu, Z. Kong and Y. Duan, Anisotropies in elastic properties and thermal conductivities of trigonal TM2C (TM = V, Nb, Ta) carbides, *Solid State Sci.*, 2019, **98**, 106027.

108 M. M. Hossain, et al., Influence of Se doping on recently synthesized NaInS2-xSex solid solutions for potential thermo-mechanical applications studied via first-principles method, *Mater. Today Commun.*, 2021, **26**, 101988.

109 X. Q. Chen, H. Niu, D. Li and Y. Li, Modeling hardness of polycrystalline materials and bulk metallic glasses, *Intermetallics*, 2011, **19**, 1275–1281.

110 Y. Tian, B. Xu and Z. Zhao, Microscopic theory of hardness and design of novel superhard crystals, *Int. J. Refract. Met. Hard Mater.*, 2012, **33**, 93–106.

111 Z. T. Y. Liu, X. Zhou, D. Gall and S. V. Khare, First-principles investigation of the structural, mechanical and electronic properties of the NbO-structured 3d, 4d and 5d transition metal nitrides, *Comput. Mater. Sci.*, 2014, **84**, 365–373.

112 Z. T. Y. Liu, X. Zhou, S. V. Khare and D. Gall, Structural, mechanical and electronic properties of 3d transition metal nitrides in cubic zincblende, rocksalt and cesium chloride structures: A first-principles investigation, *J. Phys. Condens. Matter*, 2014, **26**, 025404.

113 X. Zhou, D. Gall and S. V. Khare, Mechanical properties and electronic structure of anti-ReO3 structured cubic nitrides, M3N, of d block transition metals M: An ab initio study, *J. Alloys Compd.*, 2014, **595**, 80–86.

114 Y. Zhang, X. Yang and P. K. Liaw, Alloy design and properties optimization of high-entropy alloys, *Jom*, 2012, **64**, 830–838.

115 S. Lyu, W. Li, Y. Xia, Y. Chen and A. H. W. Ngan, Effects of chemical randomness on strength contributors and dislocation behaviors in a bcc multiprincipal element alloy, *Phys. Rev. Mater.*, 2023, **7**, 1–10.

116 J. Li, K. Yamanaka and A. Chiba, Significant lattice-distortion effect on compressive deformation in Mo-added CoCrFeNi-based high-entropy alloys, *Mater. Sci. Eng., A*, 2022, **830**, 142295.

117 S. I. Rao, Atomistic Simulations of Dislocations in a Model BCC Multicomponent Concentrated Solid Solution Alloy, *Acta Mater.*, 2017, **125**, 311–320.

118 F. Maresca and W. A. Curtin, Theory of screw dislocation strengthening in random BCC alloys from dilute to "High-Entropy" alloys, *Acta Mater.*, 2020, **182**, 144–162.

119 Q. J. Li, H. Sheng and E. Ma, Strengthening in multi-principal element alloys with local-chemical-order roughened dislocation pathways, *Nat. Commun.*, 2019, **10**, 1–11.

120 C. Lee, et al., Temperature dependence of elastic and plastic deformation behavior of a refractory high-entropy alloy, *Sci. Adv.*, 2020, **6**, 1–12.

121 F. Wang, et al., Multiplicity of dislocation pathways in a refractory multiprincipal element alloy, *Science*, 2020, **370**, 95–101.

122 S. Mu, S. Wimmer, S. Mankovsky, H. Ebert and G. M. Stocks, Influence of local lattice distortions on electrical transport of refractory high entropy alloys, *Scr. Mater.*, 2019, **170**, 189–194.

123 H. Meng, et al., Influence of Local Lattice Distortion on Elastic Properties of Hexagonal Close-Packed TiZrHf and TiZrHfSc Refractory Alloys, *Phys. Status Solidi B*, 2021, **258**, 1–9.

124 S. min Zheng, W. qiang and S. qing Wang, Elastic properties of high entropy alloys by MaxEnt approach, *Comput. Mater. Sci.*, 2018, **142**, 332–337.

125 J. He and T. M. Tritt, Advances in thermoelectric materials research: Looking back and moving forward, *Science*, 2017, **357**, 6358.

126 H. Ma, X. Zhang and F. Wang, First-principles study of the lattice vibration, elastic anisotropy and thermodynamical properties of Tantalum Silicide with the different crystal structures, *Vacuum*, 2021, **191**, 110410.

127 Y. Shen, D. R. Clarke and P. A. Fuierer, Anisotropic thermal conductivity of the Aurivillus phase, bismuth titanate (Bi4Ti3O12): A natural nanostructured superlattice, *Appl. Phys. Lett.*, 2008, **93**, 1–4.

128 D. R. Clarke, Materials selections guidelines for low thermal conductivity thermal barrier coatings, *Surf. Coating. Technol.*, 2003, **163–164**, 67–74.

129 D. G. Cahill, S. K. Watson and R. O. Pohl, Lower limit to the thermal conductivity of disordered crystals, *Phys. Rev. B*, 1992, **46**, 6131–6140.

130 D. T. Morelli and G. A. Slack, High lattice thermal conductivity solids, *High Therm. Conduct. Mater.*, 2006, 37–68.

131 X. Y. Li, et al., Observation of High-Frequency Transverse Phonons in Metallic Glasses, *Phys. Rev. Lett.*, 2020, **124**, 1–6.

132 R. Knura, T. Parashchuk, A. Yoshiasa and K. T. Wojciechowski, Origins of low lattice thermal conductivity of Pb 1 − x Sn x Te alloys for thermoelectric applications, *Dalton Trans.*, 2021, **50**, 4323–4334.

133 J. Feng, et al., Electronic structure, mechanical properties and thermal conductivity of Ln2Zr2O7 (Ln = La, Pr, Nd, Sm, Eu and Gd) pyrochlore, *Acta Mater.*, 2011, **59**, 1742–1760.

134 A. Sarkar, et al., High-Entropy Oxides: Fundamental Aspects and Electrochemical Properties, *Adv. Mater.*, 2019, **31**, 1970189.

135 D. Berardan, A. K. Meena, S. Franger, C. Herrero and N. Dragoe, Controlled Jahn-Teller distortion in (MgCoNiCuZn)O-based high entropy oxides, *J. Alloys Compd.*, 2017, **704**, 693–700.